0 0 0 0 4 1 0 3 1 2 2

LBL-3097
c1

STUDY OF AN ISOLATED, LASER-PRODUCED DEUTERIUM PLASMA IN A MAGNETIC FIELD

Thomas R. Jarboe
(Ph. D. thesis)

July 1974

Prepared for the U.S. Atomic Energy Commission
under Contract W-7405-ENG-48

For Reference

Not to be taken from this room

LAWRENCE BERKELEY LABORATORY
UNIVERSITY OF CALIFORNIA
BERKELEY

LBL-3097
c1

DISCLAIMER

This document was prepared as an account of work sponsored by the United States Government. While this document is believed to contain correct information, neither the United States Government nor any agency thereof, nor the Regents of the University of California, nor any of their employees, makes any warranty, express or implied, or assumes any legal responsibility for the accuracy, completeness, or usefulness of any information, apparatus, product, or process disclosed, or represents that its use would not infringe privately owned rights. Reference herein to any specific commercial product, process, or service by its trade name, trademark, manufacturer, or otherwise, does not necessarily constitute or imply its endorsement, recommendation, or favoring by the United States Government or any agency thereof, or the Regents of the University of California. The views and opinions of authors expressed herein do not necessarily state or reflect those of the United States Government or any agency thereof or the Regents of the University of California.

0 0 0 0 4 1 0 8 1 2 3

STUDY OF AN ISOLATED, LASER-PRODUCED DEUTERIUM PLASMA IN A MAGNETIC FIELD

CONTENTS

Abstract 1

Introduction 2

I. History of Other Work with Laser-Produced Pellet Plasmas 4

A. Work Done on Laser Pellet Interaction and Freely Expanding Plasma 4

B. Work Done in a Magnetic Field 9

II. Simple Models 12

A. Model of Plasma Formation and Free Expansion (Early Times) 12

B. Models of Expansion in a Magnetic Field 21

III. Experimental Results and Comparisons to Simple Models 26

A. Free Expansion 26

B. With Magnetic Field 29

Summary and Conclusions 34

Acknowledgments 35

Appendices 36

I. Calculation of Pellet Density During Burn 36

II. Calculation of Attenuation Distance in Dense Pellet 38

III. Calculation of Potential Energy of Conducting Sphere in $\vec{B}$ Field 39

IV. Calculations of the Expansion of a Spherically Symmetric Shell in a $\vec{B}$ Field 41

V. Calculation of the Expansion of a Shell with Density Asymmetry. 45

VI. Experimental Apparatus and Procedures. 47

A. Pellet Producer. 7

B. The Giant Pulse Ruby Laser 54

C. Pellet Detection and Laser Firing System 55

D. Magnetic Field and Vacuum Systems. 58

E. Diagnostics. 58

References 60

ABSTRACT

Apparatus is described which produces 50 μ deuterium pellets. The pellets are sliced from a continuously spun solid deuterium thread at a rate of up to 10 pellets/sec. The methods of thread production, slicing, and pellet collimation are discussed. Techniques for detection and irradiation, on one side, of these freely falling pellets with a fast rising ruby laser pulse is also described. It is found that the freely expanding plasma has an asymptotic density distribution which is shell like. The observed burn time, expansion velocity, and asymptotic density distribution are found to be in good agreement with a simple model of the burning and acceleration of the pellets. The total number of ions produced is $\sim 5 \times 10^{15}$ consistent with complete ionization of the 50 μ pellets. The plasma is given on the order of 100 eV per particle when the laser energy flux is 10^{12} watts/cm^2.

This plasma is also created in a magnetic field and its total mass and energy are measured by a large non-interacting magnetic loop probe and is found to be consistent with that measured by a large charge collector. The plasma motion perpendicular to the magnetic field is arrested with little or no actual plasma bouncing observed. This strong damping seems to be caused by either turbulent mixing or anomalous resistivity or both.

The plasma appears to be elongated in the direction of the laser beam and the flux exclusion of the plasma is seen to decrease by only a factor of about 2 immediately after peak. These effects seem to be caused by the initial density asymmetry and are shown to be consistent with a simple asymmetric expansion model.

INTRODUCTION

Since the invention of the giant pulse laser, scientists have been studying the interaction of intense laser light with matter. Laser-produced plasmas can be made by focusing the light in a dense gas[1] or by focusing it onto solid matter. Laser-produced plasmas have been made with thin and thick foils[2,3] as well as with small pellet targets. In a thick target the laser does not "burn" through the material as it does in thin targets. In "pellet plasmas" the focal spot size of the laser is larger than the target size but for laser produced "foil plasmas" the focal spot size is smaller than the target.

The advantage of laser-produced plasmas over others is that they can be very pure. The advantages of pellets over foil and gas targets are that the plasma produced is isolated and can be nearly fully ionized.

In our experiment 50 μ deuterium pellets are used as the targets for laser irradiation. Some of the advantages of hydrogen or its isotopes as the pellet material are the following: the plasma requires less energy to fully ionize, it loses less energy through line radiation and bremsstrahlung, its recombination and ionization rates are known, and since it has only one stage of ionization, one can count ions by simply measuring charge.

Deuterium pellets of 100-400 μ size have been produced and irradiated.[4,5,6] However, in order to get a fully ionized plasma of greater than 100 eV ions, using a 10 J laser, it is necessary to use smaller pellets.

Uses for laser-produced pellet plasmas other than the study of the

interaction of the plasma with the magnetic field include confinement studies,[7] line-tying experiments, instability study, and shock studies. Laser-produced plasmas trapped in a magnetic field can also be used as targets for neutral beam injection.[8] Another, more ambitious, use of laser plasma is the creation of miniature thermonuclear explosions by compressing and heating pellets (~ 0.5 mm in diameter) with high-power lasers.[9]

None of the experiments reported to date have used truly isolated pure solid hydrogen pellets freely falling in a vacuum and small enough to become fully ionized. It is the purpose of this experiment to produce and irradiate such pellets, to obtain a better understanding of their conversion into a fully ionized plasma, and to observe the early phases of expansion of the resulting plasma cloud with and without a pre-existing initially uniform magnetic field. The principal features of the experimental arrangement are most easily recognized with the help of Fig. 0.

Chapter I contains a discussion of the important studies that have been made of the laser interaction with LiH pellets. I will also discuss what work has been done related to the interaction of these plasmas with a magnetic field. In Chapter II some simple models are presented of the laser pellet interaction and the plasma interaction with a uniform magnetic field. In Chapter III these models are compared to experimental results.

I. HISTORY OF OTHER WORK WITH LASER-PRODUCED PELLET PLASMA

A. Work Done on Laser Pellet Interaction and Freely Expanding Plasma

The following is a summary with comments on what I consider to be the important work done in the area of heating and free expansion of laser-produced pellet plasmas. Most of the experimental studies have been done with LiH pellets that are suspended in a vacuum by ac electric fields.

A. F. Haught, D. H. Polk, and W. J. Fader have extended a model first proposed by Dawson[10] for the heating and expansion of laser pellet plasmas[11-13] and have compared it to their experiments.[11,13] In this hydrodynamic model the inverse bremsstrahlung absorption is computed for each volume element of the plasma. The total absorbed energy is distributed to all the particles in the plasma through a spacially independent source term in the energy equation. Because of this artificial redistribution of energy, the plasma assumes a Gaussian density profile quickly and maintains it throughout the expansion. Thus, a similarity expansion can be used even during the heating which simplifies the calculation considerably. Haught et al. found that the thermal conductivity term in the energy equation had little effect and was subsequently dropped. Indeed, it would be inconsistent to keep it since, in effect, an infinite thermal conductivity is used in the above described redistribution of absorbed energy.

In the free-expansion case, Haught and Polk, using time-of-flight measurements, have found good agreement between experiment and theory for the energy of the plasma as a function of the pellet size and laser pulse width and amplitude. However, the measured asymptotic radial density

distribution is not in agreement with the theory. The latter predicts a gaussian asymptotic density profile while a more shell-like profile was observed.[13] Three-body recombination was suggested by Haught and Polk,[13] but they concluded that this was not sufficient to account for the low density observed in the center. It also does not explain the discrepancy at large distances from the origin.

This failure to predict a shell-type expansion can be traced to the invalid assumption of uniform temperature. It was based on the fact that "...the thermalization time is significantly less than the plasma expansion time."[11] Even though this statement is marginally true, it is not strong enough to justify the use of the spacially uniform source term in the energy equation.[11,12] The necessary condition to be met is

$$W \ll KrT \ , \tag{1}$$

where W is the absorbed laser power, K is the thermal conductivity, r is characteristic dimension of the plasma, and T is the temperature. This inequality states that the temperature drop necessary to transport the absorbed laser power across the plasma is small compared to the temperature of the plasma. Now, using Spitzer's K as Haught and Polk did[11] and using their computed results,[13] we get $30 < W/KrT < 10^5$ during the time when W is above 10^{14} ergs/sec. This means inequality (1) is not satisfied during any of this time. Thus, the use of a spatially independent source term is not justifiable.

The reason the observed radial density profile is more shell-like than predicted by the theory can be explained as follows. Intuitively, where the plasma has the higher radial velocity it will also be less

dense. Consequently, since the heating per electron is proportional to the density, the regions of high density and low radial velocity will be heated more. This leads to larger radial acceleration of the low velocity regions and less acceleration of the high velocity regions than predicted. Thus, a more uniform radial expansion velocity and therefore a more shell-like asymptotic density profile is observed. A detailed model using zero thermal conductivity is presented in Chapter II. The asymptotic density profile predicted by this model is indeed shell-like.

One would expect that the infinite-conductivity assumption would tend to make the predicted absorption higher than observed since the dense regions, where most of the absorption takes place, are artificially cooled and thus remain more absorbing because of the temperature dependence of inverse bremsstrahlung. The good agreement can possibly be explained by the fact that Dawson's absorption coefficient which Haught et al. used is in error by a factor of two,[14] thus giving an offsetting error. Lubin[15] et al also did a study of the freely expanding plasma. They measured the average energy per particle by arrival times at charge collectors and the peak electron temperatures during laser heating by the use of a separate laser scattering experiment. Their heating laser was Nd glass and their diagnostic laser was ruby. Measuring T_e was difficult, but by fitting the scattering data to scattering theory, values of T_e and n_e were found. The peak T_e and the average energy per particle were found to be in good agreement with Haught and Polk's theory, especially for pellets under 20 μ diameter. Unfortunately, a comparison between the density at peak T_e was not shown. One interesting feature of Lubin's experiment is that it used a foot on the laser pulse to preheat the pellet

which allowed it to expand so that the main heating pulse could be incident at the time of optimum absorption.

Although Haught and Polk's model has its weaknesses, I am not aware of any better model for laser heating at these power levels. It is, no doubt, a good model for small pellets. From Lubin's data the theory appears to work well for pellets under 25 μ in diameter. Mattioli and Veron have shown that the model does not seem to fit the experimental heating of 50 μ and larger diameter LiH pellets.[16] They have shown experimentally that a square pulse of 20 ns length at 1.5×10^{12} W/cm^2 is required to "burn through" a 50 μ diameter LiH pellet and that a 40 ns pulse is not long enough for a 120 μ diameter pellet at 1.5×10^{12} W/cm^2. These pellets were held on the end of a quartz fiber 2 μ in diameter. They also show that the expansion is spherically symmetric if, and only if, the pulse is long enough to burn through the pellet. This demonstrates that for these large pellets the temperature does not rise uniformly and heating is not spherically symmetric. They tried using a burning model developed by Caruso and R. Gratton[17] but did not find good quantitative agreement with the burn time. They concluded that more work needs to be done on the theory of heating.

Another contribution that Mattioli and Veron have made is a fairly complete spectroscopic study of their laser-produced plasma.[18,19,20] They have also done calculations based on the theory of N. M. Kuznetsoz and Yu. P. Raizer[21] concerning the recombination of the freely expanding plasma. The calculation is oversimplified, since it does not take into account local recombination but averages over the whole plasma. They did, however, get semi-quantitative agreement with measured recombination of their

experiments. They make the observation that for plasmas with expansion velocities on the order of 10^7 cm/sec the degree of ionization does indeed become frozen and "...recombination is not important and a highly ionized plasma is collected far away from the target."[16] This seems to be true for laser plasmas produced from thick carbon targets as well as LiH pellet plasmas.[2]

A description of the interaction of a ruby laser at $\phi = 10^{12}$ W/cm^2 with a 50 μ deuterium foil is given by P. Mulser, R. Sigel, and S. Witkowski.[22] Qualitatively this description also applies to a pellet hit from one side. The model is a hydrodynamic model with inverse bremsstrahlung as the heating mechanism.

When the laser intensity exceeds 10^{10} W/cm^2 the front of the foil becomes opaque. Because of the high power absorbed, the plasma pressure becomes quite large, causing a shock to propagate through the pellet at 2.7×10^6 cm/sec. The density of the shocked material is nearly four times solid density n_0. Qualitatively, the density profile of the foil is shown in Fig. 1b. The transition for critical density n_c (the density at which the plasma frequency equals the laser frequency) to the shock density n_s occurs in a distance very small compared to the pellet size. The ideal gas law is used everywhere because solid deuterium is very compressible. P. Mulser et al also note that only a small fraction of the energy absorbed is given to the shocked material (8%).

In addition to the above work, P. Mulser, R. Sigel, and S. Witkowski have done some numerical simulations of the interaction of a laser with a 100 μm deuterium pellet. The model is again a hydrodynamic model with inverse bremsstrahlung as the heating mechanism for a power flux equal

to 5 x 10^{12} W/cm^2. Essentially all the absorption takes place in a region small compared to the dimensions of the pellet near n_c. For power less than 5 x 10^{12} W/cm^2 most of the energy incident on the pellet is absorbed. This computer simulation also includes thermal conductivity, and it was found that for $\phi < 10^{13}$ W/cm^2 thermal conductivity is of little importance in the heating process. Incidentally, this work of Mulser et al. contains 116 references to work done in laser plasma.

B. Work Done in a Magnetic Field

There have been several efforts to make a laser-produced pellet plasma in a magnetic field. In most of these experiments, the objective was to investigate the confinement of the plasma and to determine if such a plasma could be used to fill magnetic wells. Thus, much of the emphasis in these experiments has been on measuring the decay of these plasmas in the various magnetic configurations. Therefore, some experimental and theoretical work has been done on the initial stopping and capture of the laser-produced plasma.

Bernstein and Fader[23] give a theoretical treatment of the very early stages of expansion of laser-produced plasma in a magnetic field. The results are two-dimensional and are almost completely analytic. They only require a computer to do numerical integrations. The main simplifying assumptions are:

a) there is a uniform temperature,

b) the magnetic field does not affect the dynamics of the expanding plasma, and

c) the plasma is a self-similar expansion.

Assumptions b) and c) probably hold true early in time. Their results

describe the diffusion of magnetic field into the plasma. Obviously, in light of assumptions b) and c) these results do not apply during the stopping of the plasma by the magnetic field. M. L. Lubin, H. S. Dunn, and W. Friedman[15] have used this theory to compute the infrared component of the radiation due to the induced currents in the plasma. They have found agreement between the measured I.R. radiation and what was predicted.

Haught, Polk, and Fader[24] do a spherically symmetric calculation for the expansion of a laser-produced plasma in a magnetic field. It is basically a hydrodynamic calculation with a JB volume force term which represents the J x B force term. For the values of J and B they use the $\phi = \pi/2$ value of J x B of the Bernstein and Fader[23] calculations. They did not investigate in much detail experimental agreement with their model. They did, however, take some magnetic loop data and found that the signals looked something like the theory predicted.

Bhadra[25] also did a spherically symmetric calculation which has a uniform temperature. The spherically symmetric "magnetic field" is allowed to diffuse into the plasma through a skin depth parameter. Because of the assumption of spherical symmetry, the above two models cannot be expected to be useful much after the first stopping of the expansion.

Poukey[26] has done a calculation for the expansion of a superconducting shell in a uniform magnetic field which is two-dimensional. Another two-dimensional calculation was done by Lindemuth and Killeen.[27] They have done a more complete magnetohydrodynamic calculation of the expansion of the laser-produced plasma into a uniform magnetic field. The code is rather complete and includes separate electron and ion temperatures. However, it requires a background plasma and is in Eulerian coordinates.

The problem is more suited for Lagrangian coordinates, since the plasma dimensions change by several orders of magnitude during the expansion. Unfortunately, the background plasma has a mass of about one-third the mass of the pellet. The calculation is carried out to the first radial stopping of the plasma, and Lindemuth et al. show that there is almost complete field exclusion with densities and temperatures much higher near the plasma magnetic interface than in the center. From the magnetic probe measurement of their LiH laser-produced pellet, G. G. Dolgov-Savel'ev and V. N. Karnyushin[28] found that almost complete exclusion of the field occurs. Haught and Polk also state that they have a $\beta=1$ capture in the initial stopping. Experimentally, very little "bouncing" is observed by Haught and Polk[24] and G. G. Dolgov-Savel'ev and V. N. Karnyushin.[28] Tuckfield and Schwirzke[29] observed several oscillations of radial and longitudinal boundaries of luminosity in a plasma produced by the irradiation of a quartz fiber. But their attempt to correlate this "bouncing" to magnetic probe signals is not convincing.

II. SIMPLE MODELS

A. Model of Plasma Formation and Free Expansion (Early Times)

In light of the above comments on the role of thermal conduction pertaining to heating of the pellet by a laser, it seems that a model using zero thermal conductivity may better describe the laser pellet interaction. To construct such a model, I will divide it into the following time sequence: (A) early, (B) intermediate, and (C) late. The early time starts with irradiation and ends when the shock reaches the back of the pellet. The intermediate time ends when the pellet becomes translucent to laser light, and the late time is from translucency to transparency, the end of absorption. In the following discussion of the detailed physics of the over-dense plasma ($n > n_c$) I will use one-dimensional models. This is justifiable because radial expansion is greatly suppressed by the presence of the laser beam. As the dense plasma (henceforth called the pellet) tries to expand laterally across the laser beam, the density on the edge drops and the interface of laser absorption extends back as in Fig. 2. Thus a pressure due to ablation is applied also to the sides and impedes radial expansion.

(A) Early Time

A simple semi-quantitative description of the early interaction of a 50 μ deuterium pellet with a ruby laser at intensities ~ 10^{12} W/cm^2, can be made by using the assumptions listed below. a), b), and c) are supported by the results of Mulser et al.[22] described above.

a) All of the absorption takes place in a distance short compared to the pellet dimensions near $n = n_c$.

b) All of the energy incident on the pellet is absorbed, and thermal conduction is ignorable.

c) The energy going into the shocked material is small compared to the total amount absorbed in the pellet frame of reference.

d) Ionization energy and radiated energy are negligible.

e) All phases of deuterium obey the ideal gas law.

f) The only forces on the plasma are hydrodynamic in nature.

g) The deflagration of the pellet due to the laser is a Chapman-Jouguet deflagration[30] (the strongest possible).

In a Chapman-Jouguet deflagration, the burn front observed from the burned material moves at the sound speed of the burned material.[30] Thus in the pellet frame the energy flux leaving the pellet is

$$\left(\frac{1}{2} m_i C_c^2 + \frac{3}{2} kT_c\right) n_c C_c = \phi_L \ . \tag{2}$$

where m_i = mass of ion, $T_c = T_i + T_e$ at n_c, and C_c is the sound speed at the point where the density is near but less than n_c. ϕ_L = laser energy flux and is assumed constant. Since

$$C_c = \sqrt{\gamma \frac{KT_c}{m_i}} \quad (\gamma = \tfrac{5}{3}), \qquad C_c = \left(\frac{5}{7} \frac{\phi_L}{n_c m_i}\right)^{1/3} . \tag{3}$$

From Bernoulli's law and (2),

$$V_{ex} = \sqrt{\frac{14}{5}}\, C_c \tag{4}$$

where V_{ex} is the final velocity of the evaporated plasma in the pellet frame. The pressure applied to the pellet is

$$P_s = n_c kT_c + n_c m_i C_c^2 = \frac{8}{5} n_c m_i C_c^2 \ . \tag{5}$$

The velocity of the shock (see Fig. 1b)

$$V_s = V_{sm}\left(\frac{n_s}{n_s - n_o}\right) \quad \text{(conservation of mass)}, \tag{6}$$

where V_{sm} = velocity of the shocked material.

$$P_s = n_o m_i V_{sm} V_s \qquad \text{(momentum conservation)}. \tag{7}$$

$$P_s V_{sm} = \left(\frac{1}{2} m_i V_{sm}{}^2 + \frac{3}{2} kT_s\right) V_s n_o \tag{8}$$

(conservation of energy),

where $T_s = (T_i + T_e)$ in the shocked material.

$$P_s = n_s kT_s \qquad \text{[from assumption (e)]} \tag{9}$$

Combining (7), (8), and (9) yields

$$P_s V_{sm} = \frac{1}{2} V_{sm} P_s + \frac{3}{2} \frac{P_s}{n_s} V_s n_o \ .$$

Now, using (6) gives as expected

$$n_s = 4n_o \ . \tag{10}$$

Now from (10) and (6),

$$V_s = \frac{4}{3} V_{sm} \tag{11}$$

and from (7) and (8),

$$\begin{aligned} n_o m_i V_s V_{sm}{}^2 &= \left(\frac{1}{2} m_i V_{sm}{}^2 + \frac{3}{2} kT_s\right) V_s n_o \\ \therefore \frac{1}{2} m_i V_{sm}{}^2 &= \frac{3}{2} kT_s \end{aligned} \tag{12}$$

Now from (5), (7), and (11),

$$\frac{8}{5} n_c m_i C_c^{\,2} = n_o m_i \frac{3}{4} V_s^{\,2} \;;$$

thus:

$$V_s = \sqrt{\frac{32 n_c}{15 n_o}}\, C_c \qquad \text{and} \qquad V_{sm} = \sqrt{\frac{6 n_c}{5 n_o}}\, C_c \;.$$

Define

$$V_b = \frac{n_s}{n_o} \times \text{(propagation velocity of the burning front into the dense pellet)} \;;$$

from mass conservation:

$$V_b = \frac{n_c}{n_o} C_c \;.$$

From (12) the velocity of sound in the shocked material is

$$C_s = \sqrt{\gamma \frac{kT_s}{m}} = \sqrt{\frac{2}{3} \frac{n_c}{n_o}}\, C_c \;.$$

Finally, the time to burn through the pellet is

$$t_b = \frac{L_o}{V_b} \;, \tag{13}$$

where L_o is the initial length of the pellet. The shock propagation for a time t_s and

$$t_s = \frac{L_o}{V_s} \;,$$

the density of the pellet at $t = t_s$ is shown in Fig. 1c. At this point about 1/8 of the pellet is ablated. Note that the original shape of the pellet is relatively unimportant since the shock-compressed material is

in a fluid state and presumably acquires a smooth surface quickly. Moreover, the material is flattened by the strong compression so that the one-dimensional model may represent a fair approximation.

(B) Intermediate Time

Since there is a vacuum on the left end of the pellet, a complete rarefraction forms with the front edge travelling at $3C_s$ forward.[30] This simple wave propagates back through the compressed pellet with velocity C_s and finally reaches the deflagration region (see Fig. 3). The density and velocity of the plasma as a function of distance at this time are given by Courant and Friedrichs.[30] At this point about 18% of the pellet is gone and the problem becomes more difficult. However, I have solved the problem numerically by using the results of Courant and Friedrichs as the initial conditions and the boundary condition that the pressure is constant and the pellet is ablating at the rate necessary to maintain this pressure. Thermal conductivity is ignored and the adiabatic law is used. The results are shown in Fig. 4. Some artificial damping as described in Appendix I was added to suppress numerical instabilities. However, the calculation with no damping was fairly stable up to $t/t_b = 0.3$. The squares in Fig. 4a show the results of the undamped calculations, which are almost identical to the damped calculation.

(C) Late in Time

After $t/t_b = 0.9$ the thickness of the pellet (full width at half maximum of the density) is about 1 wavelength. Thus the pellet becomes translucent (see Appendix II), leading to volume absorption much as described by Haught and Polk.[11] The acceleration stops, resulting in a

three-dimensional rapid expansion of the pellet and it soon becomes transparent.

The quantity which is of the most practical significance and one of the most measurable is the asymptotic* density distribution of the plasma produced by such an interaction. The problem of finding the density distribution in space becomes tractable if the deformations of the pellet described above are ignored and the pellet is assumed hard, in the sense that the velocity is uniform throughout the pellet. If this is the case then the velocity of the pellet is described by the well known rocket formula

$$V_p = V_{ex}\, f \ln(1 - \frac{t}{t_b}) \ , \tag{14}$$

where

$$f = \frac{\int_0^\pi n(\theta_p)\, V(\theta_p) \cos\theta_p \sin\theta_p \, d\theta_p}{V_{ex} \int_0^\pi n(\theta_p) \sin\theta_p \, d\theta_p}$$

is the fraction of the ablation flux transferring momentum to the pellet along the beam direction. The distance the pellet goes is

$$\int_0^{t_b} V_p dt = \int_0^1 f\, V_{ex} t_b \ln(1 - \tau_b) d\tau_b = f\, V_{ex}\, t_b \tag{14a}$$

Now,

$$L_o = V_b t_b = \frac{n_c}{n_o} C_c t_b \ ,$$

---

*By asymptotic I mean $t_o \gg t_b$. t_o is the time of observing the density distribution. The shape is then independent of t_o, and the expansion is self-similar.[21]

so $$f\,V_{ex}t_b = f\sqrt{14/5}\;C_c t_b = f\sqrt{14/5}\;n_o/n_c\,L_o.$$

$n(\theta_p)$ is the number of ions per steradian per second going into the angle θ_p with velocity $V(\theta_p)$ in the pellet frame. In order to compare V_p to the velocity of the deflagration front in the lab frame of the previous model, $f\cdot V_{ex}$ must be set equal to 8/5 C_c. The plot of the velocity of the deflagration front of both models is shown in Fig. 5. For $0.2 < t/t_b < 0.9$ both models give essentially the same result. Thus the hard pellet model gives a good approximation to the velocity of the deflagration front in the lab frame. The greatest differences occur early in time. While the pellet is being shock compressed and while the rarefaction wave is propagating toward the deflagration front, it travels with constant velocity V_{sm}. After the rarefaction reaches the deflagration front it is rapidly accelerated as the pellet is again compressed but in a more adiabatic fashion. To proceed with finding the density distribution under this hard pellet assumption, I will first make the parameters dimensionless by normalizing all velocity to V_{ex}, which is the velocity of the plume relative to the pellet back toward the laser. $\tau_b = t/t_b$, where t is the time during pellet burning. θ_L = angle in the lab frame with respect to the laser beam and axial symmetry about the laser beam is assumed. Also assumed is that $V(\theta_p)$ and $n(\theta_p)$ are time independent so that f is constant.

From geometry,

$$V(\theta_p)\,\sin\theta_p = V_r\,\sin\theta_L\ , \tag{15}$$

$$V_r\,\cos\theta_L = V(\theta_p)\,\cos\theta_p + V_p\ , \tag{16}$$

$$V_r = r/t_o\ , \tag{17}$$

V_r = radial velocity in the lab frame.

Now define $N(\theta_p) \equiv n(\theta_p)t_b$

and write

$$N(\theta_p)\, 2\pi \sin\theta_p\, d\theta_p\, dt_b = N(\theta_p)\, 2\pi \sin\theta_p\, J_1\, d\theta_p\, dV_r$$

$$= N(\theta_p) \frac{V_r}{V(\theta_p)} dV_r\, 2\pi \sin\theta_L\, d\theta_p\, J_1$$

$$= \frac{N(\theta_p)}{V(\theta_p)} V_r\, 2\pi \sin\theta_L\, d\theta_L\, J_1 J_2\, dV_r$$

$$= \frac{N(\theta_p)}{V(\theta_p)} \frac{r}{t_o} J_1 J_2 J_3 \cdot 2\pi \sin\theta_L\, d\theta_L\, dr\ .$$

Thus

$$n(r,\theta_L) = \frac{N(\theta_p)}{V(\theta_p)\, t_o r} J_1 J_2 J_3 \quad ,$$

$$J_1 = \left.\frac{\partial \tau_b}{\partial V_r}\right|_{\theta_p} \quad ;$$ squaring (15) and (16) and adding gives

$$V_r^{\,2} = V^2(\theta_p) + V_p^{\,2} + 2V(\theta_p)\, V_p \cos\theta_p$$

So $$V_r dr = (V_p + V(\theta_p) \cos\theta_p) \frac{dV_p}{d\tau_b} d\tau_b\ .$$

From (16), $dV_r = \cos\theta_L \dfrac{dV_p}{d\tau_b}$,

thus $$J_1 = \frac{1}{\cos\theta_L} \frac{1}{\dfrac{dV_p}{d\tau_b}}$$

and from (14),

$$\frac{dV_p}{d\tau_b} = -f\,\frac{1}{1-\tau_b} \qquad \text{and} \qquad e^{V_p/f} = 1 - \tau_b \;;$$

$$\therefore\; J_1 = -\,\frac{e^{V_p/f}}{f\,\cos\theta_L} \quad .$$

$$J_2 = \left.\frac{\partial\theta_p}{\partial\theta_L}\right|_{V_r} \;;\; \text{from (15),}$$

$$\left[\frac{dV(\theta_p)}{d\theta_p}\,\sin\theta_p + V(\theta_p)\,\cos\theta_p\right] d\theta_p = V_r\,\cos\theta_L\,d\theta_L \;,$$

$$\therefore\; J_2 = \frac{V_r\,\cos\theta_L}{\dfrac{dV(\theta_p)}{d\theta_p}\,\sin\theta_p + V(\theta_p)\,\cos\theta_p} \quad .$$

Finally, $$J_3 = \left.\frac{\partial V_r}{\partial r}\right|_{\theta_L} = \frac{1}{t_o} \;,$$

$$\therefore\; n(r,\theta_L) = \frac{N(\theta_p)\,e^{V_p/f}}{V(\theta_p)\,f\left(\dfrac{dV(\theta_p)}{d\theta_p}\,\sin\theta_p + V(\theta_p)\,\cos\theta_p\right)}\;\frac{1}{t_o^3} \;, \tag{18}$$

where θ_p, f, and V_p are implicit functions of r and θ_L through Eqs. (14), (15), (16), and (17) and $V(\theta_p)$ and $N(\theta_p)$ are given.

If for example

$$n(\theta_p) = 1 \qquad 0 \leq \theta_p < \pi/2$$
$$ = 0 \qquad \pi/2 \leq \theta_p \leq \pi$$

and

$$V(\theta_p) = 1 \;.$$

The asymptotic density distribution is shown in Fig. 6a.

Also the time of arrival of plasma to a probe is

$$t = \frac{R}{V_r}, \qquad \text{where } R = \text{distance of probe.}$$

Now

$$\frac{N(\theta_p)}{V(\theta_p)} V_r \, 2\pi \sin\theta_L \, d\theta_L \, dV_r \, J_1 J_2 = \frac{N(\theta_p)}{V(\theta_p)} \frac{R}{t} 2\pi \sin\theta_L \, d\theta_L \, dt \, J_1 J_2 J_3' ,$$

$$J_3' = -\frac{R}{t^2} .$$

Thus ∴

$$I = \frac{N(\theta_p)}{V(\theta_p)} \frac{1}{\tau^4} \frac{1}{f} e^{V_p/f} \frac{d\Omega_L}{\frac{dV(\theta_p)}{d\theta_p} \sin\theta_p + V(\theta_p) \cos\theta_p} , \qquad (19)$$

where $\tau \equiv \frac{t\, V_{ex}}{R}$ and $d\Omega_L$ is the solid angle of the probe. These considerations are utilized in Chapter III.

B. Models of Expansion in a Magnetic Field

Early in time, before the magnetic field has an effect on the plasma, the plasma is axially symmetric about the laser beam. However, since the laser beam is perpendicular to the magnetic field, the subsequent expansion is truly three-dimensional with no axis of symmetry. In the following models the effects of the asymmetries introduced by the directional nature of the laser beam and the magnetic field are discussed. The initial mass and energy are the same in all the models.

It can be easily seen that the density distribution Eq. (18) is

shell-like for almost any reasonable $N(\theta_p)$ and $V(\theta_p)$. (See Fig. 6.) This, in conjunction with the fact that the plasma will tend to pile up on the boundary, makes it reasonable to assume that the plasma expands in a shell. In order to illustrate the effects of the two-dimensional nature of the magnetic field, I will compare the expansion of a perfectly conducting spherically symmetric shell in a magnetic field to that of one expanding against a uniform isotropic external pressure field. The value of the pressure will be $P = (3/16\pi)B_0^2$. This pressure is chosen because $P \cdot \mathrm{Vol} = 1/4\ r^3B_0^2$. This is the potential energy of a superconducting sphere of radius r in a uniform magnetic field B_0 (see Appendix III). The equation of motion then becomes

$$M \frac{d^2r}{dt^2} + \frac{3}{4} r^2B_0^2 = 0 \quad .$$

Integrating once yields:

$$\frac{dx}{d\tau} = (1 - x^3)^{1/2} \quad ,$$

where $x = r/r_m$; $\tau = tV_o/r_m$ and $r_m^3 = 2MV_o{}^2/B_0^2$, and V_o = initial expansion velocity of the sphere, and M = total mass of the plasma shell. The values of $x(\tau)$, $V(\tau)$, and $\phi(\tau)$ are found by doing the integral numerically. The results are shown in Fig. 7a, b, c, and d. $\phi(\tau)$ is the flux excluded from a loop. The initial energy of the shell is $1/2\ \mu_m B_0$, where μ_m is the maximum dipole moment and occurs when the shell is stopped, i.e., when it has reached its maximum radius r_m. The value of $\mu_m = 1/2\ r^3{}_m B_0$ is the quantity that can be determined with the magnetic loop probe. Thus r_m is found and from the definition of τ,

$$M = \frac{B_0^2}{2} r_m \left(\frac{\Delta t}{\Delta \tau}\right)^2 . \tag{20}$$

Here Δt and $\Delta \tau$ correspond to similar time intervals on the experimental and theoretical expansions. This equation shows how M depends on Δt and B_0.

Now I introduce this same conducting ball in a real magnetic field much as Poukey[26] did. However, instead of solving the equation for the stream function in terms of spherical harmonics, I approximate the shell by rings, and then adjust the currents in the rings so that the stream functions are nearly correct between the rings (see Appendix IV). This I will call Model A, for short.

Figure 7 shows the RMS value of V_r, the average value of V_z for the right half, and the flux exclusion for a loop as well as the results of the uniform isotropic pressure case. Up to the first return of the shell (all that is shown) both cases give very similar results. It is interesting to note that in this model V_z as well as V_r are stopped by the uniform $\vec{B}$ field.

The effects of diffusion and pressure due to finite conductivity as well as the effects due to the fluid nature of the plasma are added to the magnetic field calculation (see Appendix IV) and as expected[24,25] the results differ little from the perfectly conducting case when using classical conductivity. An important difference being that V_z average only decreases to one-half its initial value.

The addition of strong anomalous resistivity ($\nu_{ie} = \omega_{pi}$ added when $v_d = 4v_{ith}$) lowers the amplitude of the flux signal and destroys any stopping parallel to the field. The flux signal still goes very high

compared to the value to which it returns (see Fig. 7). It does not, however, go back to zero as in the calculation without anomalous resistivity. In fact, with only classical resistivity, at the time the plasma returns from its first bounce off of the field, the flux signal goes negative with $\vec{B}$ inside the plasma greater than $\vec{B}$ outside.

Figure 7 shows that, in the case of complete field exclusion from the shell, ignoring the directional nature of the magnetic field is a reasonably good approximation when $\tau \leqslant 2.5$. So, in order to show the effects of the density asymmetry discussed in Section I, the density distribution produced by the irradiation of a pellet is condensed to a shell and placed in a uniform isotropic pressure field. In so doing, I assume the experimental result $N(\theta_p) \propto \cos^2\theta_p$ and $V(\theta_p) = 1 - (1/3)\sin\theta_p$. Note that the axis of symmetry in this model analysis is <u>not</u> parallel to $\vec{B}$ but aligned with the laser beam. The rings here therefore do not represent current loops but mass rings subject to the isotopic external pressure. Thus, the same computer program can be used, but not all the properties of the magnetic interaction can be simulated in this calculation. However, the basic aspects of flute distortions can be incorporated in this way. This is called Model B. (See Appendix V for details of calculations.)

It is seen that in this case the rings do not have the same bounce period and are not kept in phase by the pressure representing the magnetic field. The points on the shell start at the same time but with different masses per unit area and different velocities. Consequently they are stopped at different times giving a lower peak flux exclusion, and they return to the axis of symmetry at different times giving a higher minimum after peak (see Fig. 8).

If the number of rings is ≥ 45, high β flutes begin to develop during the stopping and soon after they become fairly large causing damping of the bouncing. Figure 9 shows the time development of this interaction when 90 rings are used. The shell comes to a pseudo pressure balance with no temperature and complete field exclusion. Except for a small fraction of the shell (about 15% going forward), all points on the shell are eventually stopped by this isotropic pressure field. By stopping I mean that V_z and V_r both are equal to zero at some time during the expansion, not necessarily at the same time.

The fine grain structure that develops allows for rapid diffusion of the plasma and real pressure balance probably occurs. Enough diffusion can take place in this manner so that confinement parallel to the field becomes negligible and the plasma expands down the approximately straight field lines. In fact, this anomalous diffusion due to the fluting can be thought of as being caused by an anomalous resistivity. Certainly, the net result is nearly the same as the symmetric case with anomalous resistivity in a magnetic field. The main difference is that the plasma is elongated in the direction of laser irradiation. Also, the magnetic flux signal does not immediately return to as low a value and it does not decay to zero in the isotropic case as it does in the other. This is due partly to the fact that in the isotropic pressure case the plasma does not escape down the field lines. (Fig. 10 shows a plot of the flux exclusion in the two cases.) In all models described above the plasma is stopped by the magnetic field. However, with strong anomalous resistivity and fluid effects added, no bouncing occurs and V_r becomes negative only after $t \geq 5$ x (the time of peak flux exclusion). This is illustrated in Fig. 11 which shows the shape of the shell at several times.

III. EXPERIMENTAL RESULTS AND COMPARISONS TO SIMPLE MODELS

A. Free Expansion

The experimental apparatus and procedures used are described in Appendix VI. I will first compare the simple model of the free expansion to the experimental results. The following diagnostics are used in the free expansion: six coaxial charge collectors (Fig. 29), two photo diodes, a spectrograph, and long time exposure photographs of the zap zone.

The charge collectors are located 8 cm from the zap zone approximately on the axes of a three-dimensional coordinate system with laser light coming down one axis. Forward refers to the direction the laser light is going and back is the opposite direction. Typical probe currents are shown in Fig. 12.

An expanding density distribution which is uniform will give a current that decreases as $1/t^4$. These signals fall off faster than that. Therefore, in light of Fig. 6a, it seems reasonable to fit the data to the model given in Chapter II. Figure 13 shows the fit achieved using the hard pellet model. The fit is a least-squares fit of the probe currents to Eq. (19), with $n(\theta_p) = A \cos^{\alpha} \theta_p$ and $V(\theta_p) = V_{ex}(1 - B \sin\theta_p)$, where A, B, and α are the fitting parameters and V_{ex} is found by measuring the time of the current peak of the back probe.

$$V_{ex} \equiv R/t_p ,$$

where R = distance of the probe from the zap zone. A is a normalization constant and α and B parametrize the nature of the deflagration.

In the data analyzed (6 typical shots) the value of $\alpha = 2.0 \pm 0.3$

and B = 0.33 ± 0.06. The ± includes the full range of values found. The asymptotic density distribution from such $N(\theta_p)$ and $V(\theta_p)$ is shown in Fig. 6b.

If one assumes that the plasma comes off the pellet normal to the surface of n_c and travels in straight lines with respect to the pellet, then by using the experimentally determined $N(\theta_p)$ and $V(\theta_p)$ the shape of deflagration front can be calculated and the results are shown in Fig. 14. The shape is very similar to what would be expected from the discussion of the detailed model.

The sudden change in the rate of fall of the back signals can be understood as a consequence of the arrival of the rarefaction wave at the deflagration front. The poor fit to the forward probe signal is understood from the description of the late part of the burn. Once the pellet becomes translucent it is so thin it quickly becomes transparent. Thus, much of the forward going plasma travels at the velocity the pellet had when translucency occurred and arrives at the probe at the same time, producing the narrow spike. By comparing this pellet velocity to the exhaust velocity, the time during the burn at which translucency occurs can be measured. The relative position of the forward peak with respect to the back varies slightly from shot to shot and the times of arrival are nearly equal. Now, if $N(\theta_p) \propto \cos^2\theta_p$ and $V(\theta_p) \propto 1 - (1/3)\sin\theta_p$, then f = 37/60. The peaks arrive at about the same time; therefore, translucence occurs when $V_p = V_{ex}$. Thus

$$1 = f \ln(1 - \frac{t}{t_b}) \quad \text{or} \quad t = 0.8\, t_b \ .$$

At this point, if it were not for lateral expansion, the length of the compressed pellet would be 2.5 μ or about 3.4 free-space wavelengths. This is too thick for translucency. However, if you assume in Fig. 14 that the original pellet corresponds to the nearly vertical portion of the pellet profile, then the average pellet radius has increased about 50%. Thus the area is about doubled and the length of the pellet is halved. This would mean that the pellet is 1.7 wavelengths long at translucence, which is a more reasonable value. It appears to be necessary that the pellet expand before radial confinement can be accomplished.

The two photo diodes are calibrated by the use of an optical calorimeter. The difference of the input and output photo diodes is used to measure the burn time, and the amplitude of the input is used to measure the laser power. Fig. 15 shows the graph of Eq. (4) for V_{ex} as a function of ϕ_L along with measured values of V_{ex} and ϕ_L. There seems to be reasonably good agreement here. Fig. 16 shows the laser pulse output and the difference signal. The measured absorption time is about 16 ns. Taking into account the radial expansion described above and substituting numbers into Eq. (13), I get

$$t_b = 7.2\ \phi_L^{-1/3}\ \text{ns} \qquad (\phi_L \text{ is in } 10^{12}\ \text{W/cm}^2)$$

Now, since the absorbed power is 11.8 MW, $\phi_L = 0.2 \times 10^{12}$ and so the expected t_b = 12 ns. Thus, the model and experiment are consistent.

Incidentally, if LiH is the pellet material and Nd glass is used for the laser then $t_b = 22\ \phi_L^{-1/3}$ ns. So for 50 μ pellets at $\phi_L = 1.5 \times 10^{12}$, t_b = 19 ns. This is in good agreement with the experimental

results of Mattioli and Veron.[16]

It would be interesting to observe the deflagration front with a streak or fast framing camera, but simply taking a long time exposure photograph of the burn can serve to measure the distance the pellet goes. Typical photos are shown in Fig. 17. By averaging the length minus the width of the white part of the photographs and then taking the magnification and the angle of observation into account, I find the average measured translation of the pellet during the burn to be .4 ± .15 mm. Using the simple model and the assumptions that the burning stops at τ_b = .8, that L_0 = 25 μ (because of radial expansion), and that f = 37/60, I get the calculated translation of .42 mm. I chose the above shots more or less at random among the good lases ($\phi \approx 10^{12}$). Finally, the spectrograph of the plasma showed only hydrogen lines demonstrating that the plasma is indeed pure.

B. <u>With Magnetic Field</u>

The principal diagnostics used in studying the plasma's expansion in the uniform magnetic field are magnetic loop probes, a large area charge collector, and a plasma camera. The plasma camera and charge collector are described in Appendix VI.

The most interesting magnetic loop data is taken by the use of a 4.5 cm diameter loop which is centered on the zap zone. The loop is rotated slightly from normal to the magnetic field to allow the pellets to fall through it and to allow the laser beam to hit the pellets. The voltage from the loop is integrated using a 22 μs passive integration. Typical signals from this probe are shown in Fig. 18 for both 4.0 and 7.0 kG shots.

Early in time, from t=0 to the peak of the signal, it looks qualitatively like any and all of the simple models presented in Chapter II. The most interesting feature is that the flux signal begins to drop rapidly as expected after the peak but then stops rather abruptly between 1/3 and 2/3 of its peak value. The signal then decays slowly to zero.* From this can be concluded that the plasma bouncing is highly damped and can best be described either by Model A, with a strong anomalous resistivity, or Model B, which has asymmetric initial density distribution. These are not really competing models but each contribute to an understanding of the expansion.

Model B shows what happens to the cross sections perpendicular to the field lines while Model A shows what happens parallel to the field lines. The strong anomalous resistivity put in A can be thought of as a convenient way to take into account the turbulent damping illustrated by B.

Fitting the experimental data to the simple theory is done by the use of two parameters, the mass and the energy of the expanding plasma. The strength of the anomalous resistivity could also be used as a fitting parameter. However, I have not used it and its strength remains as stated in Chapter II.

The flux signals seen at 4.0 kG fit fairly well to Model A. Figure 10 shows the normalized experimental data plotted with the expected results from Model A and B. Generally in the lower field data the signals

---

*The rate of this decay is what is expected from a one-dimensional adiabatic expansion of the plasma down the field lines with $\gamma = 5/3$.

return to a relatively lower value after the peak, and, although the stop is still more abrupt than Model A, it is not as abrupt as in the higher field shots. That the lower field shots are better described by A than the higher field shots may be due partly to the fact that the burn time of the pellet (~ 16 ns) becomes a larger fraction of the stopping time (~ 53 ns at 7.0 kG, ~ 68 ns at 4.0 kG). The finite burn time causes the expansion to become even more asymmetric. This enhancement of the asymmetry in the direction of the laser beam due to the $\vec{B}$ field is also shown by the plasma camera photographs. Figure 19 shows typical shots at 4.0 and 7.0 kG. For the 7 kG data, the overexposed part where most of the plasma arrives has a shape very much like that of Fig. 9f which is expected using Model B. In the lower field shot, 4 kG or less, most of the plasma arrives in a considerably more circular area. On many shots low density flutes do appear at more or less random angles with respect to the laser beam. The plasma camera is placed 50 cm from the zap zone. The field lines that go through the zap zone go through the center of the plasma camera and are perpendicular to it. The radii of the circular lines are in 1 cm increments.

Another reason why the 7.0 kG flux exclusion signal looks more like Model B may be due to the fact that the gyro orbits are smaller at higher fields and thus the plasma is probably more susceptible to fluting. The effects of adding more rings in Model B seem to be similar to the effects of adding more field in the experiment.

By fitting the experimental data to Model B, the mass and energy of the plasma can be measured. The mass and energy are independently measured by collecting the ions with a large charge collector. Only one charge collector placed 16 cm from the zap zone is used. It was found from

preliminary measurement that when two charge collectors were used the charge arriving at each one was essentially the same. The energy is measured by observing the current as a function of time, then computing the root mean square velocity, the velocity being measured by the time of arrival at the charge collector. The mass is simply m_i/e times the total charge collected.

The best shot-to-shot correlation* between the two methods is found when the loop data is normalized such that the size of the flux peaks is made equal to that of Model B and the time of the sudden change in slope after the peak (t_n) is made equal to the first minimum after the peak in Model B. When this normalization is made, the mass found by using the loop data is 1.37 ± 0.16 times the mass measured using the charge collectors for 7.0 kG shots and 1.04 ± 0.09 for 4.0 kG shots. The corresponding energy ratios are 1.13 ± 0.27 for 7.0 kG and 1.28 ± 0.08 for 4.0 kG. The number after the ± is the calculated root mean square deviation for 12 shots at 7.0 kG and 6 shots at 4.0 kG. The above shot-to-shot variation is within experimental error. The values measured by the loop probe are larger than when measured by the charge collector. This may be expected because three loop probes were between the zap zone and the charge collector at the time these data were taken. However, they were all centered on the field lines that pass through the zap zone so most of the plasma could pass through them. Another explanation is that the 16 ns burn time can cause an overestimate of the mass of up to 30% in the 7.0 kG case.

---

*By best shot-to-shot correlation I mean the "fractional deviation" is minimal. The "fractional deviation" is the value behind the ± divided by the average.

There is a mystery which I will leave unresolved, and it is the following: by computing the integral of the current monitoring signal, the charge collected appears to be about 0.58 ± 0.07 of the amount that is found by measuring the voltage drop directly. In both the mass and energy comparison, the shot-to-shot fractional deviation is lower, using the mass computed from the directly measured voltage drop. Therefore, I used this value of the mass in the above summary of results, and the current signal is used only to measure the RMS velocity.

The average value of t_n at ~ 7.2 kG is 93 ns and at 4.0 kG is 127 ns, verifying that $t_n \propto B^{-2/3}$, as the simple model predicts. The average number of ions is $5.2 \pm 2.1 \times 10^{15}$ which is consistent with the approximately 6×10^{15} that is in the pellet. The average energy per ion is on the order of 100 eV. A table of these shots is shown in Table 1.

Finally, coaxial charge collecters were used to observe the plasma escaping perpendicular to the magnetic field. The plasma collected was orders of magnitude less than with B=0. This, in addition to the fact that most of the plasma is collected by the large charge collector, shows that the perpendicular motion of the plasma is indeed arrested by the magnetic field.

SUMMARY AND CONCLUSIONS

We have made and irradiated on one side, freely falling 50 μm deuterium pellets with a fast rising ruby laser pulse. It was found that the freely expanding plasma had an asymptotic density distribution which was shell like. The burn time, expansion velocity, and asymptotic density distribution were found to be in good agreement with a simple model of the burning and acceleration of the pellet.

This plasma was also created in a magnetic field and its total mass and energy was measured by a large non-interacting magnetic loop probe and was found to be consistent with that measured by a large charge collector. The plasma motion perpendicular to the magnetic field was arrested with little or no actual plasma bouncing observed. This strong damping seemed to be caused by either turbulent mixing or anomalous resistivity, or both.

The plasma seemed to be elongated in the direction of the laser beam and the flux exclusion decreased by only a factor of ≈ 2 immediately after the peak. These effects seemed to be caused by the initial density asymmetry and were consistent with a simple asymmetric model. The plasma did approach low-β conditions probably within three or four "stopping" times ($\equiv 1.4\ r_m/V_o$). The field lines then became approximately straight with the plasma, having a cross section of dimensions $\gtrsim r_m$, adiabatically expanding along them.

ACKNOWLEDGMENTS

The author wishes to thank Wulf B. Kunkel and William R. Baker for their advice and encouragement during the course of the work. Special thanks are extended to Allan Lietzky for his cooperation in designing, constructing, and operating this experiment. The author also wishes to thank L. Biagi, K. W. Ehler, J. Galvin, E. B. Hewlett, V. J. Honey, M. Fitzgerald, and G. Rankin for their technical assistance. The author also wishes to thank his wife, Colleen F. Jarboe, for her assistance in the writing of this thesis.

This work was performed under the auspices of the U. S. Atomic Energy Commission.

APPENDIX I: CALCULATION OF PELLET DENSITY DURING BURN

The calculation is done very simply. The initial density and pressure distribution are given by Courant and Friedrichs,[30] and the boundary condition is that the pressure at the deflagration is constant. After each time-step, the appropriate fraction of the slab at the deflagration is removed to simulate the ablation.* The density distribution is divided into 100 equal mass slabs. The pressure between the slabs is computed using the adiabatic law with $\gamma = 5/3$. The slab's motion is governed by the equation $\rho \frac{dV}{dt} = -\nabla P$.

Thermal conduction is ignored because the thermal relaxation time of the dense pellet is much longer than the burn time. Assuming that the temperature of the pellet is 1 eV, then the fractional ionization from Saha's equation is $\approx 10^{-4}$. Thus the heat is conducted primarily by atoms or molecules. From simple dimensional arguments

$$t_{relax} = \frac{n\sigma_0}{\overline{V}} \ell^2 \quad .$$

Unfortunately $\sqrt{\sigma_0} \approx d$, the average spacing between the atoms. However, I don't expect this to cause an error of many orders of magnitude. So with $n = 10^{23}/cm^3$, $\sigma \approx 10^{-15}$ cm^2; $\overline{V} \approx 10^6$ cm/sec, and $\ell \approx 10^{-3}$ cm

$$t_{relax} \approx 10^{-4} \text{ sec} \gg t_b \quad .$$

---

*Due to an algebraic error the value of C_s used to find the boundary conditions is $\sqrt{2}$ too large. This should not change the results significantly.

The calculation is slightly unstable and is stabilized as follows. The pressure should monotonically decrease away from the boundary condition of constant pressure. So if $P_i > P_{i-1}$, then the velocities on both sides of P_i are set equal to their average and two-thirds of the excess energy goes to thermal energy, which increases P_{i-1} and one-third goes to increase P_i. Using this damping mechanism, the calculation conserves energy to within 1%.

APPENDIX II: CALCULATION OF ATTENUATION DISTANCE IN DENSE PELLET

Some energy must be deposited in the plasma very near n_s in order that this density can decrease to n_c without causing a rarefaction wave to propagate into the pellet. Such a rarefaction is not allowed because P_s is maintained by the deflagration process.

By substituting numbers into Eqs. (9) it is found when $\phi = 10^{12}$ watts/cm^2, $T_s = 1.6$ eV. From Saha's equation it is found that $n_e = 4.8 \times 10^{20}/\text{cm}^3$. Now, using 10^{-15} cm^2 (Ref. 31) as the electron-neutral scattering cross-section it is found that $\nu_{ei} = 2 \times 10^{16}$. Using these values the energy attenuation length is given by Kunkel[32] to be $\approx 3\ \lambda_0$.

From a similar calculation at positions closer to the deflagration front the attenuation length is found to become as short as $\lambda_0/10$. Therefore one would expect the pellet to become translucent at lengths on the order of λ_0.

APPENDIX III: CALCULATION OF POTENTIAL ENERGY OF CONDUCTING SPHERE IN $\vec{B}$ FIELD

The following is a derivation of the change in magnetic field energy of an infinite uniform field due to the introduction of a perfectly conducting sphere of radius a and uniform B_{in} inside.

The currents in the sphere produce a dipole external field.[33] The sphere can be thought of as being inside a perfectly conducting larger sphere with the larger sphere radius eventually allowed to go to infinity. The currents on the larger sphere cancel the dipole field of the smaller. Thus the field created by these currents <u>inside</u> the larger sphere is uniform and has the value of $B_D \frac{a^3}{R^3}$, where R is the radius of the larger sphere and

$$B_D = B_{out} - B_{in} ,$$

where B_{out} is the field outside of the smaller sphere minus the dipole field produced by it.

$$B_{out} = B_0 + B_D\left(\frac{a}{R}\right)^3 ,$$

where B_0 is the initial uniform field in the large superconducting sphere before the small one is introduced. Now, the fields outside of the small sphere produced by the currents in it are

$$B_r = \frac{a^3 B_D \cos\theta}{r^3} ,$$

$$B_\theta = \frac{a^3 B_D \sin\theta}{2r^3} .$$

So, all the field energy inside the large sphere is

$$\int \frac{B^2}{8\pi}\, d\,\mathrm{Vol} = \frac{B_{in}^2}{8\pi} \cdot \frac{4\pi a^3}{3} + \int_a^R \int_{-1}^1 (B_\theta^2 + B_r^2)\, 2\pi r^2\, d\cos\theta\, dr =$$

$$= \frac{B_{in}^2 a^3}{6} + \int_a^R \int_{-1}^1 \left(\frac{B_D a^3 \sin\theta}{2r^3} + B_{out} \sin\theta\right)^2 +$$

$$+ \left(\frac{B_D a^3 \cos\theta}{r^3} - B_{out} \cos\theta\right)^2 2\pi r^2\, d\cos\theta\, dr =$$

$$= \frac{B_{in}^2 a^3}{6} + \frac{1}{4}\left[\frac{1}{3} B_D^2 a^6 \left(\frac{1}{a^3} - \frac{1}{R^3}\right) + \frac{2}{3} B_{out}^2 (R^3 - a^3)\right].$$

Now $\quad \Delta E_{mag} = \int \frac{B^2}{8\pi}\, d\,\mathrm{Vol} - \frac{B_0^2 R^3}{6}$.

The facts that $B_0 = B_{in} + B_D(1 - \frac{a^3}{R^3})$ and $B_{out} = B_{in} + B_D$ and some algebra yield

$$\Delta E_{mag} = \frac{1}{4} B_D^2\, a^3 (1 - \frac{a^3}{R^3}) .$$

Thus if $R \to \infty$, $\quad \Delta E_{mag} = \frac{a^3 B_D^2}{4}$

A similar calculation for the case of an infinitely long cylinder gives the result $\Delta E_{mag/unit\ length} = r^2/8 \cdot B_D^2$.

APPENDIX IV: CALCULATIONS OF THE EXPANSION OF A SPHERICALLY SYMMETRIC SHELL IN A $\vec{B}$ FIELD

The following is a description of the calculation used to simulate the expansion of a shell in a magnetic field. Also included is an explanation of the modifications to the calculation which approximates heating and diffusion as well as the fluid nature of the plasma.

The stream function for the set of rings is

$$\psi(r,z) = -B_0/r^2 + rA_i(r,z) \quad ,$$

where r and z are cylindrical coordinates and $A_i(r,z)$ is the ϕ component of the vector potential of the ith ring. The value $A_i(r,z)$ is found in the literature.[33] The value of $\psi(r,z)$ on the shell with a uniform field inside is

$$\psi(r,z) = B_{in}r^2/2 \ .$$

The stream function is made to approximate this value at two points on the shell between adjacent rings. Thus, there are twice as many fitting points as there are rings. A least-squares fit is used to adjust the currents to make $\psi(r,z)$ close to the proper value at these points.

Each ring has a v_z and v_r, and the force on the ring is found by assuming that the current in the ring is distributed over an area halfway to the adjacent rings on both sides. w is the width of this region and $w^2 = (\Delta r)^2 + (\Delta z)^2$. The "area" of the ring is then $2\pi rw$. The magnetic force on a ring with a current I is easily found by considering superposition of magnetic fields. B_{in} can be thought of as being everywhere

in space and then the rest of the field, B_{ex}, is parallel to the shell at its boundary. Its magnitude from Ampere's law is

$$B_{ex} = \frac{4\pi I}{wc} .$$

Thus the force on the ring due to this field (see Fig. 20) is

$$f_1 = 2\pi r \; I \; B_{ex}/2c$$

The factor of 2 in the denominator is needed because the average value of the field in the shell is $\vec{B}_{ex}/2 + \vec{B}_{in}$.

Now $$f_{1r} = -f_1 \sin\theta = -f_1 \frac{\Delta z}{w}$$

and $$f_{1z} = -f_1 \frac{\Delta r}{w}$$

and the force due to the uniform B_{in} is

$$f_{2r} = \frac{-2\pi r \; I \; B_{in}}{c}$$

and $$f_{2z} = 0 .$$

Thus the total force on the ring is

$$f_r = \frac{-4\pi^2 r \; I^2 \; \Delta z}{c^2 w^2} - \frac{2\pi r \; I \; B_{in}}{c} ,$$

$$f_z = \frac{-4\pi^2 r \; I^2 \; \Delta r}{c^2 w^2} .$$

For the calculation with infinite conductivity and no fluid effects,

$$B_{in} = 0 .$$

Extending this model to take into account diffusion makes it necessary to include pressure because of the heating caused by diffusion. The pressure force on the shell at each ring is found as follows. Each ring is thought of as distributed over a volume proportional to its area such that the sum of the ring "volumes" is equal to the actual volume. All of the rings' volumes are assumed to reach the z axis and have the same temperature. The force on a ring due to the pressure in its volume acts outward on its area ($2\pi rw$) and the pressure difference of adjacent rings in the z direction acts on the area (πr^2) of the ring. The amount of heating or cooling due to compression or expansion is simply the sum of the PdVs of the rings.

The heating and diffusion is done as follows. It is assumed that the amount of heating is the same as occurs in a segment of an infinite cylinder in a magnetic field. The segment has the same length and maximum diameter as the shell. The current density is made constant for convenience so that the dissipation is simply $\eta\, j^2 \times$ (volume occupied by current). The value of j is set such that $\int_0^{r_m} B_D^2\, dA$ is the same as in the shell because the rate of energy dissipation is closely related to the energy stored (see Appendix III). This dissipation increases the pressure and causes diffusion. B_{in} increases the amount necessary to lower the energy stored in the magnetic field by an amount that is equal to the energy dissipation in the ohmic heating. The energy stored is assumed to be $B_D^2/8\pi \cdot 2z_m\, \pi r_m^2$, where z_m and r_m are the maximum of z and r on the shell. From Appendix III it can be seen that this is exactly true for both the sphere and the long cylinder.

The diffusion is computed between time steps. The currents are

recomputed and the shell moves. During movement the flux inside the plasma is held constant. Thus, B_{in} can increase or decrease depending on what dominates, expansional decrease or diffusive increase.

Further improvements can be made by allowing the plasma to accumulate in the shell during expansion instead of it all being there initially. This is done by starting with a small fraction of the mass in the shell and the rest experiencing a self-similar expansion inside the shell. When the shell is slowed by the magnetic field, the plasma on the inside hits the shell and suffers a perfectly inelastic collision with it. The excess energy goes into heat. Thus the shell's mass increases with time until all of the plasma is collected. This mass accumulation is done in the r direction only. The total mass is used all of the time for the dynamics in the z direction. The density distribution used for the self-similar expansion is that of the back going plasmas in the free expansion calculation.

In summary, the mass is concentrated in a shell and is given an initial velocity outward and is spherically symmetric. (It need be only axially symmetric, with the axis of symmetry parallel to the magnetic field.) The forces on the shell arise from the $j \times B$ forces of the currents in the shell with the magnetic field, from the pressure from within the shell, and from inelastic collision of the fluid which is expanding inside the shell. The temperature is increased by ohmic heating, by collision of the fluid with the shell, and by compression. A flow diagram for the computation is given in Fig. 21.

APPENDIX V: CALCULATION OF THE EXPANSION OF A SHELL WITH DENSITY ASYMMETRY

To simulate the expansion of the asymmetric density distribution against a surrounding uniform isotropic pressure, each ring is given a mass equal to

$$M_R = \frac{m_i}{e} \int_0^\infty I \, dt ,$$

where I is the current collected by a probe in the free expansion case [Eq. (19)] with $\Delta\Omega = 2\pi \sin\theta \, \Delta\theta$ and $\Delta\theta = \pi/(\text{no. rings})$ and each ring is given a radial velocity

$$V_R = \int_0^\infty \frac{R}{t} \cdot \frac{I \, dt}{\int_0^\infty I \, dt} .$$

The "area" of the ring is the same as in Appendix IV. The rings make elastic collisions with the axis of symmetry in the r direction and also elastic collision with their neighbors in the z direction.

Energy is conserved to better than 3% for the time that is shown in Fig. 9. These shapes are essentially independent of the time step or number of rings. However, if the number of rings increases, the flutes do develop earlier and get larger. The main difference in the flux exclusion is that it peaks a little earlier and at a slightly lower value and the flux signal does not decrease to as low a value after peak (see Fig. 8). This is expected because by increasing the number of rings the wavelengths available for flute growth become shorter and thus the growth rates become larger.

The purpose of this calculation is not to simulate the actual expansion but simply to illustrate the effects of flute formation and initial density asymmetry on the flux exclusion signal and to show qualitatively the elongation of the plasma's expansion in the direction of the laser beam.

APPENDIX VI: EXPERIMENTAL APPARATUS AND PROCEDURES

The apparatus used in this experiment are categorized as follows:

(A) pellet producer

(B) giant pulse ruby laser

(C) pellet detection and laser firing systems

(D) vacuum chamber and magnetic field production systems

(E) plasma diagnostics.

Pellets are produced, collimated, and allowed to fall freely in a uniform magnetic field toward the focal region of the ruby laser pulse (Fig. 22). Most of the pellets produced do not fall through this focal region. However, when a pellet is on the proper trajectory to fall through this focus, the detection system triggers the ruby laser in the proper sequence so that the laser fires when the pellet arrives at its focal region.

After the pellet is irradiated, the plasma produced expands in the uniform magnetic field (which can be set equal to zero) and is studied by the use of charge collectors, magnetic probes, and a plasma camera.

A. Pellet Producer

In the apparatus to be described, the pellets are produced by slicing a 50 μ diameter thread into 50 μ length cylinders with a thin tungsten wire. The solid thread is made by allowing liquid deuterium of the proper temperature and pressure to flow through an aperture into a vacuum. The temperature is controlled through the vapor pressure of continuously produced liquid hydrogen coolant. After being produced, the pellets are collected by a funnel and collimated by falling through a quartz capillary

tube. This method of pellet production uses no liquid helium and only a few drops of liquid hydrogen, which renders the process both safe and inexpensive (approximately 10^{-5} dollar per pellet).

The apparatus for producing 50 μ deuterium pellets consists of the following components (Fig. 23):

(1) hydrogen liquifier

(2) thread spinner

(3) thread slicer

(4) pellet collimator.

1. Hydrogen Liquifier

Bottled high-pressure hydrogen is used to produce the liquid hydrogen coolant. Hydrogen of ≈ 70 atm is cooled to 65°K (pumped liquid nitrogen) and is then allowed to expand out a counter-current heat-exchanged capillary which has no constriction at the output. Although such a constriction is generally used because it increases the effectiveness of the counter-current heat exchanging, it also increases the chance of the tube becoming plugged from the impurities in the H_2 that condense out. Here, plugging is virtually eliminated by using this straight-walled capillary and by filtering the incoming H_2 with Zeolite (Linde, 13x and 5a at 65°K). The capillary is 150 μ id and is approximately 40 cm long. Approximately 0.15 liter/sec STP of H_2 is used in the liquifier.

At first, attempts were made to spin a hydrogen thread by extruding it through a small hole in the hydrogen liquifying cavity. Hydrogen threads were actually produced by this method, but only on a transient basis.

The present system uses two separate thermally connected cavities:

one containing the coolant, the other the thread material. Thus, we can independently vary the pressure, temperature, and thread material of the extrusion cavity. The temperature can be regulated to within 0.1 K by adjusting the pressure in the liquifying cavity to the nearest 20 Torr.[34] Note that the only equipment needed for temperature regulation is a needle valve on the H_2 exhaust and a pressure gauge.

2. Thread Spinner

One of the most interesting parts of the device we call the "thread spinner." This is the tapered extrusion orifice in a 300 μ thick zone-refined copper plate. The large 100 μ opening of the orifice faces the liquid, and the smaller 70 μ opening is toward the vacuum chamber. Such a hole in any good thermal conducting material will work. For example, we have used a 6/90 ruby watch jewel. It was found experimentally that a stable thread is produced when the temperature of the copper plate and deuterium cavity is between 19 and 22°K and the cavity pressure is between 400 and 1200 Torr. The rate at which the thread is formed is about 4 mm/sec. Changing the temperature or pressure seems to have little effect on the rate of the thread formation or its diameter except near the extremes of the operating range. During normal operation the pressure is set at 500 Torr and the temperature at 21°K. A qualitative explanation of the thread spinning is shown in Fig. 24. Lines of heat flow are indicated on the left and the directions of solid, liquid, and gas movements are shown on the right. When liquid deuterium is introduced into the cavity, a plug of solid deuterium forms at the hole from the liquid that is cooled and frozen through evaporation when it is exposed to the vacuum. Liquid deuterium flows into the plug from above and solid and gaseous deuterium

flow out the bottom. As the tapered plug moves downward, the deuterium melts near the copper and is removed by pressure in the liquid layer next to the copper. Steady flow occurs when the downward force from the pressure above the plug is balanced by the upward force on the plug from the pressure in the liquid layer. This balance can be achieved by keeping the copper temperature near triple point temperature of deuterium (18.69°K) which maintains the desirable controlled distance between the solid deuterium and the copper.

The total amount of deuterium that flows into the vacuum chamber due to the thread and its production is ≈ 50 micron-liters per sec. This low pumping load is important since it allows one to easily maintain a pressure as low as $< 10^{-4}$ Torr, which is necessary because forces develop on the pellets due to gas moving between surfaces of different temperatures. These forces arise because more momentum flux is incident on the pellet from the hot surface than from the cold surface and because the pellets ablate at a greater rate on the side facing the hot surface. Both of these phenomena force the pellets toward the cold surfaces. It is conceivable that these forces could be used to collimate and/or transport the pellets, or they can be reduced by decreasing the pressure in the vacuum chamber. These forces were observed to dominate the motion of the pellets during early experiments but were made small compared to gravitational forces, by decreasing the pressure. They will be small, compared to gravitational forces, if $p \ll \rho g \ell$, where p is the chamber pressure, ρ = the pellet density, g = gravitational acceleration, and ℓ = the characteristic size of the pellet. For a 50 μ deuterium pellet, $\rho g \ell = 7 \times 10^{-4}$ Torr.

For the sake of completeness, Fig. 24 shows other modes of operation that have been observed. In the freeze-off mode (Fig. 24a) a dome of solid deuterium forms over the hole and only gas enters the vacuum chamber. This mode of operation puts out about 2000 micron-liters of gas per sec. By raising the temperature to the normal operating range, the stable thread used to make pellets forms. This dome has been observed through a transparent ruby thread spinner.

If the extrusion orifice is inverted (Fig. 24b), a thread will form, but it will move very fast. Liquid surface tension holds the thread to the copper plate. Attempts to slice the thread break this weak bond and disrupt the formation of the thread. Increase of pressure on mode (b) results in an unstable thread which is larger than the spinner hole (Fig. 24c).

The amount of deuterium flowing into the vacuum chamber while operating in any of modes a, b, or c, is more than an order of magnitude larger than the amount of deuterium introduced while making pellets. Finally, there is a mode of operation not illustrated, which is caused by too high a temperature and/or pressure. A large amount of liquid flows through the hole, forming random-sized globs of frozen deuterium. This mode of operation is called "blow-out" and generally overloads the vacuum system.

3. Thread Slicer

As a stable thread is being produced, it is sliced into pellets by a 25 μ tungsten wire which is driven past the hole perpendicular to the thread and cuts it about 25 microns from the spinner hole. The wire is

attached to a speaker coil which is driven with a 250 Hz, gated square wave. While the 250 Hz oscillation is on, the thread is vaporized at the plane of oscillation of the relatively hot wire. Pellets of desired length are extruded while the wire is stopped. Thus by adjusting the on and off time of the 250 Hz oscillation one can control the length of the pellet and the rate of pellet production.

It was found experimentally that when a 25 μ wire was passed through the thread only once, the thread remained intact. One can speculate that the wire, which is held at liquid deuterium temperature, passes through the thread causing it to liquify near the wire. This liquid flows around the wire and fuses the thread together again on the other side, much of the deuterium in the thread being evaporated at each pass. Several passes are needed to slice the thread which indicates the smoothness of the slicing method.

The slicing action is so gentle, in fact, that it can be adjusted so as not to traverse the thread completely. This causes the thread to be notched in such a way that the pellets produced are connected by a small filament of deuterium. By observing the notched thread with a microscope while operating in this manner, the length of these connected pellets can be made approximately equal to the diameter of the thread. Then the amplitude of the oscillation can be increased until the thread is completely severed, thus producing cylinders of 50 μ length and diameter. Measurement of the amount of deuterium in the pellets indicates that the length of the pellet can be adjusted to give about 3×10^{15} molecules per pellet.

4. Pellet Collimator

As one might expect, the pellets leave the slicing region with some horizontal velocity. Most of them are caught by an 8 cm diameter copper funnel, which has a 2 mm hole in the center and is liquid nitrogen cooled. A relatively flat funnel with a slope of about 20° is used because less horizontal and vertical velocity is given to the pellets in bringing them to the center. This slope is just steep enough to prevent the pellets from sticking to impurities and imperfections in the funnel surface. A low vertical velocity is desirable because the pellets will then have a longer time in the collimating tube to lose its horizontal velocity.

After leaving the funnel, the pellets fall through a 3-mm-id quartz capillary tube, also held at LN temperature. (Quartz is used because it is essential that the interior wall of the tube be clean and smooth.) This tube is broken into 10, 15, and 20 cm segments to allow for the escape of gas from the pellets. The length and diameter of the segments allows sufficient gas conductivity to prevent gas build-up in the tube.

The following conditions must be satisfied so that pressure does not build up in the tube: $C \gg NRAv_s$, where C is the conductivity of the tube. N is the maximum number of pellets in the tube, R is the number of molecules liberated by the collision of a gas molecule with pellets, A is the total area of the pellet, and v_s is the thermal velocity of gas in the tube. If this inequality is not satisfied, gas will evaporate from the pellet in the tube at a greater rate than can be exhausted by the tube. Thus, there will be an exponential increase of the gas pressure in the tube that will blow pellets out of either end of the tube, usually with considerable horizontal velocity, and the pellets will not be

collimated.

This inequality is satisfied for the capillary tubes used to collimate the pellets. The pellets seem to fall parallel to the tube and are distributed over the cross-sectional area of the tube. If the pellets are produced at the rate of 10/sec, then the incident rate of pellets in the focal region of the ruby pulse laser is ≈ 1/min. The last segment of the collimating tube also provides vacuum isolation of the pellet production chamber. The pellets are detected and irradiated 10 cm below the collimating tube.

B. The Giant Pulse Ruby Laser

The pulse laser was designed and built at the Laboratory. It has an oscillator and two amplifiers and is capable of up to 10 joules output per pulse. When operated as a normal Pockel cell Q-switched laser, the pulse width is 30-50 ns. However, by use of a half glan, a laser triggered spark gap, and another Pockel cell, a pulse with less than 1 ns rise time can be made from the Q-switched pulse.

Three photo diodes which are calibrated with the help of an optical calorimeter are used as laser diagnostics. One monitors the oscillator cavity, another monitors the output of the two amplifiers. This is called the input photo diode since it monitors the light incident on the pellet. The third photo diode monitors the light coming out of the zap region. This is called the output photo diode. The balanced difference of the input and output photo diodes tells when absorption and/or scattering takes place. The difference is taken on a 454 Tectronics scope and the input pulse appears on the same trace with the circuit shown in Fig. 28. The

circuit starting at the 50 Ω "Y" is equivalent to a 170 ns open ended cable except that there is 50% attenuation in the reflected signal. A typical different signal and the input photo diode signal is shown in Fig. 26.

C. Pellet Detection and Laser Firing Systems

The detection system senses when a pellet is on the proper trajectory to enter the focal region of the giant ruby pulse laser (henceforth called the zap zone). Two signals are then generated. The first signal triggers the flash lamps which pump the ruby for about 0.8 msec before the pellet enters the zap zone. The second one triggers the Pockel cell which Q-switches the laser causing it to lase at the moment the pellet passes through the center of the zap zone. A vertical laser beam which is smaller than the zap zone shines through it and illuminates the pellets (see Fig. 22). A 1 mw HeNe laser was used but there was barely enough scattered light. We are now using an 18 mW HeCd laser and the scattered light is ample. The vertical beam is focused by the use of three lenses. Two are spherical and one is cylindrical. Because an effective focal length of 10 cm is needed and the access window is more than 10 cm from the zap zone, two spherical lenses are used to expand the beam and focus it 2.75 mm above the zap zone. This 10 cm effective focal length system is needed because the detector laser's beam divergence is about 1 mrad and a focal spot of 100 μ is necessary in order to resolve that the pellet is well within the 200 μ diameter of the zap zone. The cylindrical lens is used to turn the point focus into a line focus. The line focus is parallel to the ruby laser beam and is about 0.5 mm long. Thus the area into which a detectable

pellet can fall is increased by a factor of five over what a point focus would give. The change in the power per cm^2 of the giant pulse laser along this line is less than 20%. The length of the line focus is Df_s/fc, where D is the diameter of the incoming vertical laser beam before it hits any lens, f_c is the focal length of the cylindrical lens, and f_s is the focal length of the spherical lens system. It is interesting to note that the line length is independent of the position of the cylindrical lens as long as it is the first lens the detection beam hits.

Since the pellets' trajectories are very nearly parallel straight lines, those that go through this line focus will also go through the zap zone provided that the detection laser beam is made parallel to these trajectories. The scattered light from the illuminated pellets is collected at 90° to the detection beam and about 30° to the ionizing ruby laser beam and is focused on a set of three slits (Fig. 22). The images of the slits on the vertical beam are approximately 3.0, 2.5, and 0.1 mm above the zap zone. The height of each image is approximately 0.1 mm. The light from all three slits goes into one photomultiplier. When a pellet falls down the vertical beam the output consists of three pulses, as shown in Fig. 26. The signal passes through a band pass filter which suppresses photomultiplier noise and noise from flash lamp lights.

To eliminate large differences in amplitude, the signals are logarithmically compressed and then fed into the laser firing logic (Fig. 27). If the peak of the first signal is high enough, a 100 μsec flash window is generated when the second pulse is expected (approximately 200 μs after the peak of the first pulse). If the peak of the second pulse occurs during this flash window and is of sufficient amplitude, then a signal is

sent which fires the flash lamp, and a zap window is generated when the final pulse is expected to arrive, about 0.8 msec later. When the third pulse appears in the zap window, a properly delayed signal is sent to actuate the lasing of the ruby laser by Q-switching the oscillator cavity.

Although the primary reason for the two upper slits is to distinguish the light scattered in the upper slit from that scattered in the lower, the requirement of two properly spaced signals prior to the flash lamps being fired helps to insure that the pellet is on the proper trajectory to go through the zap zone. Since commitment to use the laser occurs at the firing of the flash lamps, the line focus of the detection beam is placed between the image of the upper two slits. By using this detection scheme we have been over 95% successful in making an expanding deuterium plasma each time the flash lamps are fired.

The vertical beam and slits are aligned by the following procedure. A foil is placed in the zap zone at 45% to vertical and a hole is burned in it using the ruby laser. The vertical beam is then centered on the hole and the collimating tube is adjusted to be coaxial with it. The three lenses are then put in place, the beam being recentered on the hole with the placement of each lens. Finally, the slits are adjusted so that the image of the vertical beam is perpendicular to them and the light scattered from the hole hits slightly below the last slit. At this point pellets are hit with $\vec{B}=0$. By observing the coaxial charge collecting probes described below, it is found that the faster expanding plasma leaves the pellet from the side on which it was hit. By using this charge collecting data, fine adjustments are then made in the placement of the detection beam and in the delay in the lase time with respect to the peak of the last detected

pulse, so that the irradiated pellets are at the center of the ruby laser focus. Thus, the free expansion is made axially symmetric. It is found experimentally that changes in the position of the irradiated pellet by 30 μ make marked changes in the symmetry of the free expansion.

D. Magnetic Field and Vacuum System

The magnetic field is produced by water-cooled coils and is adjustable from zero to 7.5 kG d.c. and can go as high as 20 kG pulse (30 second pulse). The solenoid is about 4 meters long and the vacuum chamber for the plasma study fits inside the solenoid and is 20 cm in diameter. A 1350 liters/sec ion pump (500 liters/sec of air) is on the chamber and a pressure of about 10^{-6} Torr is maintained while running. A much lower pressure could be easily achieved by allowing the unused pellets to fall through the plasma production chamber into another vacuum chamber for disposal. The vacuum system used on the pellet production chamber is a liquid nitrogen-trapped-diffusion pump. The two systems are isolated by the last tube of the pellet collimator.

E. Diagnostics

The free expansion diagnostics are shown in Fig. 28. More details of the photo diode arrangement for measuring the burn time are described in Section B of this Appendix. The coaxial charge collectors are simply tubular 50 Ω coaxial cables, one of which is shown in Fig. 29. The tubular coax is used as a vacuum feed through and the end is turned off smoothly. These probes are biased around 50 volts and placed 8 cm from the zap zone. It was found when placing two probes close together that both probes gave the same signal when the bias voltage on one was varied from 5 to 150 volts.

Thus, saturated ion current is being drawn. It was also found that one probe could be moved to within 4 cm of the zap zone and the same asymptotic density distribution was measured. This was not found to be the case at 2 cm. The probe at 2 cm shows less plasma produced than the one at 8 cm.

The loop probes used when the magnetic field is on are described in Chapter IV. The charge collector and plasma camera are shown in Fig. 30. The plasma camera is much like that used by Coensgen et al.[35] The large charge collector is 11 cm in diameter. The front is a 25 μ thick foil with ~ 100 μ diameter holes in it spaced every 500 μ. Its transparency is determined optically to be 3.5%. The screen and the ion collecting plate behind it are made of 304 stainless steel. Ten 0.1 μF extended foil polystyrene capacitors are used for voltage biasing and each has a 1 Ω precision resistor in series with it. The voltage of one of the resistors is measured and this is the current monitoring discussed in Chapter IV. The charge collector is biased to 50 volts and typical voltage drops produced by irradiated pellets are ~ 10 volts. Its resistance and inductance are low enough so that essentially all of the capacitor voltage always appears between the screen and the ion collecting plate.

REFERENCES

1. H. J. Schwarz and H. Hora, Laser Interaction and Related Plasma Phenomena (Plenum Press, New York - London, 1972).

2. P. T. Rumsby and J. W. M. Paul, Temperature and Density of an Expanding Laser Produced Plasma, Plasma Physics 16, 247 (1974).

3. R. Sigel, Experimental Investigation of Plasma Production by Irradiating Solid Hydrogen Foils with an Intense Pulse Laser, Z. Naturforsch 25a, 488-503 (1970).

4. U. Ascoli-Bartoli, B. Brunell, A. Garuso, A. DeAngelis, G. Gatti, R. Gratton, F. Parlamge, and H. Salzmann, Production of a Dense Deuterium Plasma in a Strong Magnetic Field (Hot-ice Experiment), in Plasma Physics and Controlled Nuclear Fusion Research (International Atomic Energy Agency, Vienna, 1969), Vol. 1, p. 917.

5. G. Francis, D. W. Atkinson, P. Avivi, J. E. Bradley, C. D. King, W. Millar, P. A. H. Saunders, and A. F. Taylor, Laser Produced Plasma from Isolated Solid Hydrogen Pellets, Phys. Letter A25, 486 (1967).

6. T. Sekiguchi, H. Hirosawa, M. Tanimoto, and A. Kitsunezak, Laser-plasma Production System from a Single Solidified Gas Particle, Journal (Tokyo University Faculty of Engineering), Series A, 36 (1968).

7. A. F. Haught, D. H. Polk, and W. J. Fader, Magnetic Field Confinement of Laser Irradiated Solid Particle Plasmas, Phys. Fluids, 13, 2842-2857 (1970).

8. A. F. Haught, D. H. Polk, J. T. Woo, W. J. Fader, R. G. Tomlinson, R. A. Jong, and W. B. Ard, High-B Capture and Mirror Confinement of Laser-Produced Plasmas, Semi-annual Report, Feb. 1 - July 31, 1973 (United Aircraft Corp. UARL-M-921514-19).

9. J. L. Emmett, J. Nuckolls, and L. Wood, Fusion Power by Laser Implosion, Scientific American 230, 24 (June 1974).

10. J. M. Dawson, On the Production of Plasma by Giant Pulse Lasers, Phys. Fluids, 7, 981 (1964).

11. A. F. Haught, and D. H. Polk, High-Temperature Plasmas Produced by Laser Beam Irradiation of Single Solid Particles, Phys. Fluids 9, 2047 (1966).

12. W. J. Fader, Hydrodynamic Model of a Spherical Plasma Produced by Q-Spoiled Laser Irradiation of a Solid Particle, Phys. Fluids, 11, 2200 (1968).

13. A. F. Haught, and D. H. Polk, Formation and Heating of Laser Irradiated Solid Particle Plasma, Phys. Fluids 13, 2825 (1970).

14. J. M. Dawson, and T. J. Johnston, Correct Values for High-Frequency Power Absorption by Inverse Bremsstrahlung in Plasma, Phys. Fluids, 16, 722 (1973).

15. M. J. Lubin, H. S. Dunn, and W. Friedman, Heating and Confinement Studies of Laser-Irradiated Solid Particle Plasmas, in Plasma Physics and Controlled Nuclear Fusion Research (International Atomic Energy Agency, Vienna, 1969), Vol. 1, p. 945.

16. M. Mattioli and D. Veron, Production of Energetic Highly Ionized Plasma by Laser Irradiation of Lithium Hydride Pellets, Phys. Fluids, 14, 717-721 (1971).

17. A. Caruso, and R. Gratton, Some Properties of the Plasmas Produced by Irradiating Light Solids by Laser Pulses, Plasma Physics 10, 867 (1968).

18. M. Mattioli and D. Veron, Electron-Ion Recombination in a Laser Produced Plasma, Plasma Physics, 11, 684 (1969).

19. W. Seka, J. L. Schwab, and C. Breton, Spectroscopic Measurement on Laser-Produced LiH Plasmas, J. Appl. Phys. 41, 3440 (1970).

20. M. Mattioli, Recombination Processes During the Expansion of Laser Produced Plasma, Plasma Physics 13, 19-28 (1971).

21. Ya. B. Zel'Dovigh, and Yu. P. Raizer, Physics of Shock Waves and High Temperature Hydrodynamic Phenomena (Academic Press, New York, 1966).

22. P. Mulser, R. Sigel, and S. Witkowski, Plasma Production by Laser, Phys. Reports (Section C of Phys. Letters), No. 3 (1973), 187-239 North-Holland Publishing Company.

23. I. B. Bernstein and W. J. Fader, Expansion of a Resistive Spherical Plasma in a Magnetic Field, Phys. Fluids 11, 2209 (1968).

24. A. F. Haught, D. H. Polk, and W. J. Fader, Magnetic Field Confinement of Laser Irradiated Solid Particle Plasma, Phys. Fluids 13, 2842 (1970).

25. D. K. Bhadra, Expansion of a Resistive Plasmoid in a Magnetic Field, Phys. Fluids 11, 234-239 (1968).

26. J. W. Poukey, Expansion of a Plasma Shell into a Vacuum Magnetic Field, Phys. Fluids 12, 1452-8, (1969).

27. I. Lindemuth and J. Killeen, Alternation Direction Implicit Techniques for Two-Dimensional Magnetohydrodynamic Calculations, Preprint UCRL-74656.

28. G. G. Dolgov-Savel'ev and V. N. Karnyushin, Expansion and Diffusion of a Laser Plasma in a Magnetic Field, Zh. Eksp. Teor. Fiz. 61, 1002 (1971).

29. R. G. Tuckfield and Schwirzke, Dynamics of a Laser Produced Plasma Expanding in a Magnetic Field, Plasma Physics 11, 11-18 (1969).

30. R. Courant and K. O. Friedrichs, Supersonic Flow and Shock Waves (Interscience Publishers, New York).

31. J. W. Bond, Jr., K. M. Watson, and J. A. Welch, Jr., Atomic Theory of Gas Dynamics (Addison-Wesley, Reading, Mass.), p. 141.

32. W. B. Kunkel, Plasma Physics in Theory and Application (McGraw-Hill, New York, 1966), p. 249.

33. J. D. Jackson, Classical Electrodynamics (John Wiley, New York - London).

34. D. B. Chelton and D. B. Mann, Cryogenic Data Book, National Bureau of Standards Cryogenic Engineering Laboratory, Boulder, Colorado, May 15, 1956 (UCRL-3421).

35. F. H. Coensgen, W. F. Cummins, W. E. Nexsen, Jr., and A. E. Sherman, Plasma Camera, Rev. Sci. Instrum. 25, 1072-1074 (1964).

Table 1. Mass and energy of the plasma measured with the loop probe and the large charge collector.

Shot No.	B field (kG)	r_m (cm)	Number of Ions		Total Energy of Plasma		Energy per Atom	
			By Loop	Loop/Coll.	By Loop (joules)	Loop/Coll.	By Loop (eV)	Loop/Coll.
437	7.36	.306	5.1×10^{15}	1.45	.039	.90	48	.77
449	7.44	.321	4.1	1.35	.046	1.22	70	.60
450	7.44	.521	9.6	1.56	.196	.83	128	.78
452	7.36	.477	9.3	1.62	.147	.78	99	.80
453	7.36	.284	3.3	1.26	.031	1.17	59	.68
455	7.36	.434	8.0	1.30	.111	1.32	88	.58
464	7.04	.369	4.0	1.22	.062	.72	97	1.13
468	7.04	.339	3.5	1.21	.048	1.35	87	.61
471	7.00	.394	5.5	1.53	.075	1.57	85	.42
472	7.00	.258	2.8	1.52	.021	1.44	47	.46
473	7.04	.256	2.3	1.14	.021	1.38	56	.63
474	7.04	.325	4.3	1.27	.043	1.11	63	.71
476	4.00	.605	3.6	1.10	.089	1.28	154	.71
477	4.00	.613	4.9	1.00	.092	1.36	117	.73
480	4.00	.803	7.5	.88	.207	1.18	174	.96
481	4.00	.615	5.0	1.09	.093	1.21	117	.76
482	4.00	.581	3.6	1.01	.078	1.40	136	.71
483	4.00	.674	6.5	1.16	.123	1.23	118	.70

FIGURE CAPTIONS

Fig. 0. Principal components of the laser-ionized pellet experiment. The high-power laser is focused on the so-called "zap-zone", on the axis of the magnet solenoid.

Fig. 1. Early stage of laser pellet interaction. The density versus x is plotted at (a) $\tau_b = 0$, (b) $\tau_b = 0.1$, and (c) $\tau_b = 0.125$. [(c) shows the end of the early time.]

Fig. 2. Qualitative shapes of the pellet for the times in the burn shown in Fig. 1. Ions ablated from the sides of the pellet produce a radial force inward which limits radial expansion. The dashed line in (b) shows the position of the shock front.

Fig. 3. After the shock propagates across the pellet a complete rarefaction wave propagates toward the deflagration front. The shape of the density profile is given in the literature.[30]

Fig. 4. After the rarefaction wave reaches the deflagration front, the "pellet" is recompressed. These density plots are found by a simple computer calculation (Appendix I). Note the dramatic shifts in the origins of the position scale.

Fig. 5. The velocity of the deflagration front in the hard pellet model compared to the more detailed calculation. Both are one-dimensional calculations.

Fig. 6. Asymptotic density distribution (a,b) for example in Chapter II, and (c,d) that were experimentally determined. (a,c) are the density distributions in the direction of the laser and (b,d) are perpendicular to the laser beam.

Fig. 7. Comparisons of the expansion of a spherically symmetric shell in an isotropic pressure and in a magnetic field. The (a) radius at the center, (b) rms v_r, (c) v_z average, and (d) the flux excluded from a loop are shown as a function of time. (———) isotropic pressure, (– – – –) perfectly conducting shell in a field, (–·–·–·) conducting shell in a $\vec{B}$ field with anomalous resistivity and fluid effects.

Fig. 8. Flux exclusion for Model B, using various numbers of rings.

Fig. 9. Time development, in an isotropic pressure, of a density distribution similar to that produced by laser irradiation of a pellet (z is in the direction of the laser beam).

Fig. 10. Flux exclusion from Model A (–·–·–·) and Model B (– – –) compared to experimental results taken at 4 and 7 kG.

Fig. 11. The shape of the shell in Model A when τ = 1,2,3,4,5, and 6.

Fig. 12. Typical signals seen by the coaxial charge collectors for B = 0. Signals show collected ion currents (inverted) as a function of time for three shots. The early small signal is due to photo emission caused by UV generated during the pellet burn.

Fig. 13. Fit of coaxial charge collection to simple theory (——) and experiment (– – – –).

Fig. 14. Average shape of the deflagration front during the pellet burn.

Fig. 15. The exhaust velocity of the laser-produced plasma as a function of laser power. The solid line is what is expected from the simple model.

Fig. 16. Burn time measurement of 50 μ deuterium pellets.

Fig. 17. Long time exposure photographs of pellet burn (see Fig. 28). The light vertical streak is due to the falling pellets which are illuminated by the detection beam. (The number is the shot number.)

Fig. 18. Flux exclusion from a 4.5 cm diameter loop due to plasma produced by the irradiation of a 50 μ deuterium pellet with a laser in a uniform magnetic field of (a) 4 kG and (b) 7 kG. (The number is the shot number.)

Fig. 19. Plasma camera photographs of the plasma as it streams into the plasma camera, which is 50 cm from the zap zone. This is a long time exposure photograph of the scintillator (see Fig. 30). (The number is the shot number.)

Fig. 20. Shape of the shell and position of ring at $\tau = 1.86$ in Model A.

Fig. 21. Flow diagram of computer program used to estimate the expansion of the plasma in a magnetic field.

Fig. 22. Pellets are detected by a vertical HeCd laser beam.

Fig. 23. Apparatus for producing laser targets of 50 μ diameter deuterium pellets.

Fig. 24. Model of the thread "spinning."

Fig. 25. Other modes of spinner operation.

Fig. 26. Photomultiplier output for a usable pellet and the time of appearance of the flash window and the zap window.

Fig. 27. Logic for firing the laser from the pellet signals.

Fig. 28. Free expansion diagnostics.

Fig. 29. The coaxial charge collector.

Fig. 30. Diagnostics used in a magnetic field.

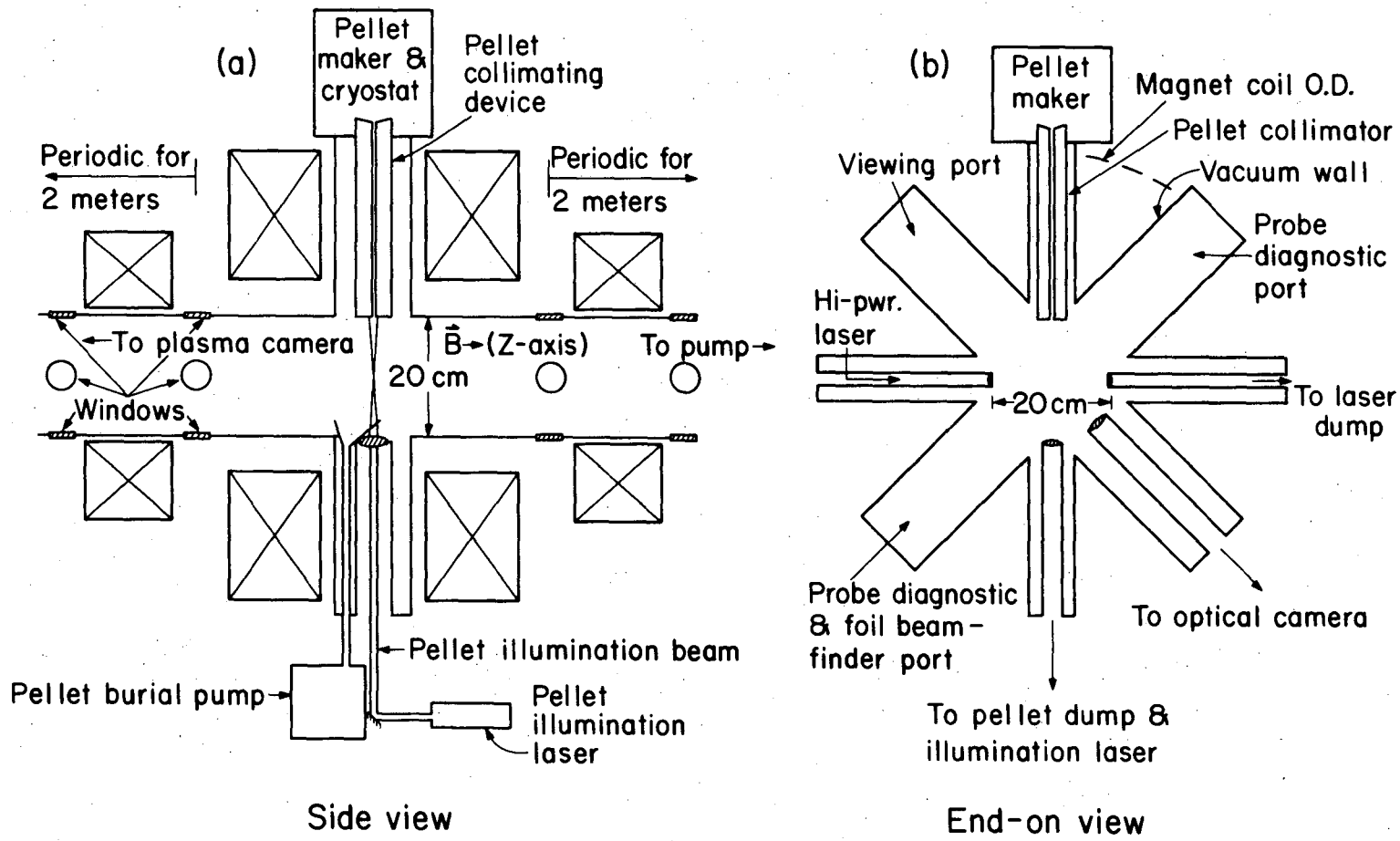
(a)
Pellet maker & cryostat
Pellet collimating device
Periodic for 2 meters
Periodic for 2 meters
To plasma camera
Windows
B (Z-axis)
20 cm
To pump
Pellet illumination beam
Pellet burial pump
Pellet illumination laser
Side view
(b)
Pellet maker
Magnet coil O.D.
Pellet collimator
Viewing port
Vacuum wall
Probe diagnostic port
Hi-pwr. laser
20 cm
To laser dump
Probe diagnostic & foil beam-finder port
To optical camera
To pellet dump & illumination laser
End-on view
XBL 749-4248

Fig. 0

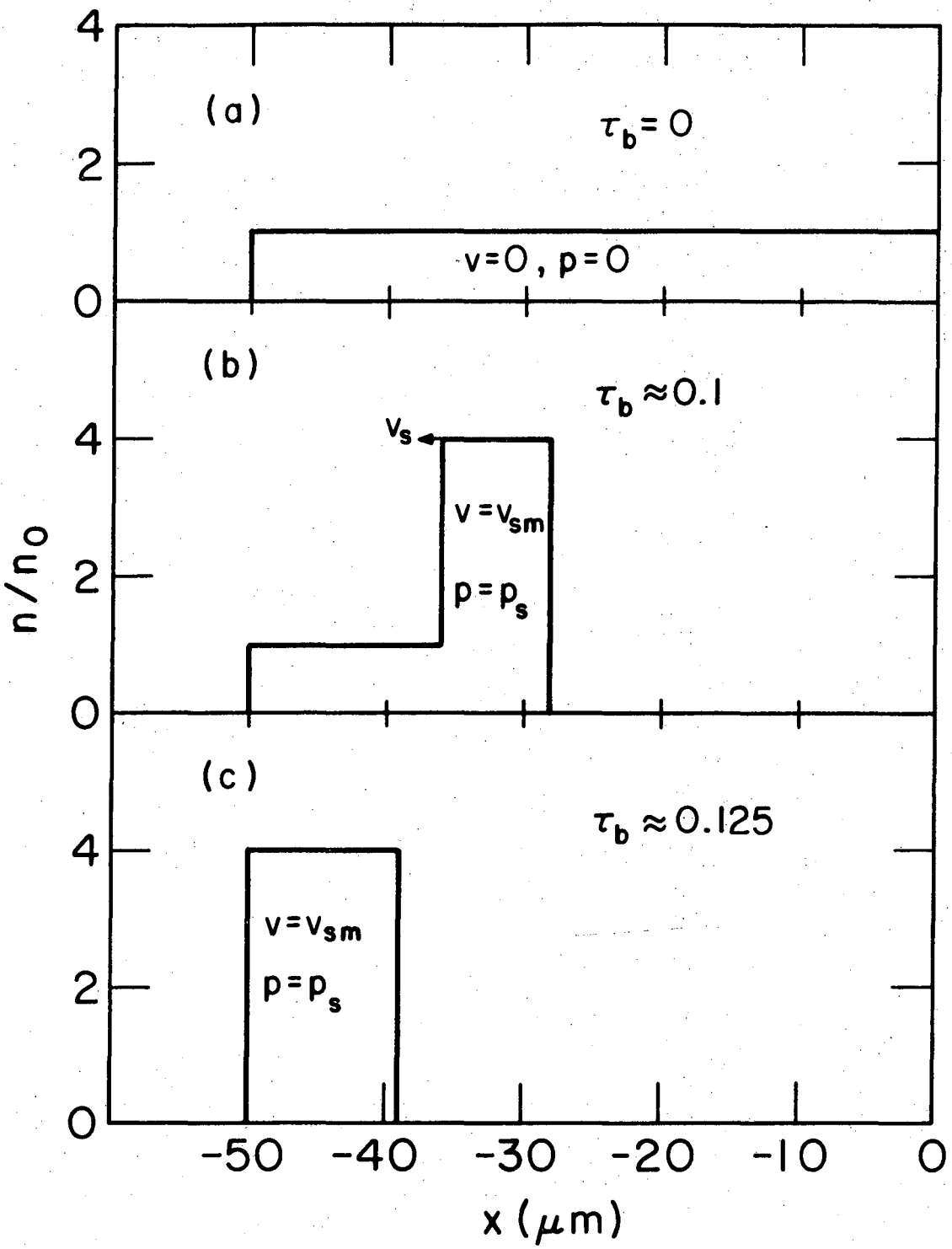

XBL 749-4200

Fig. 1

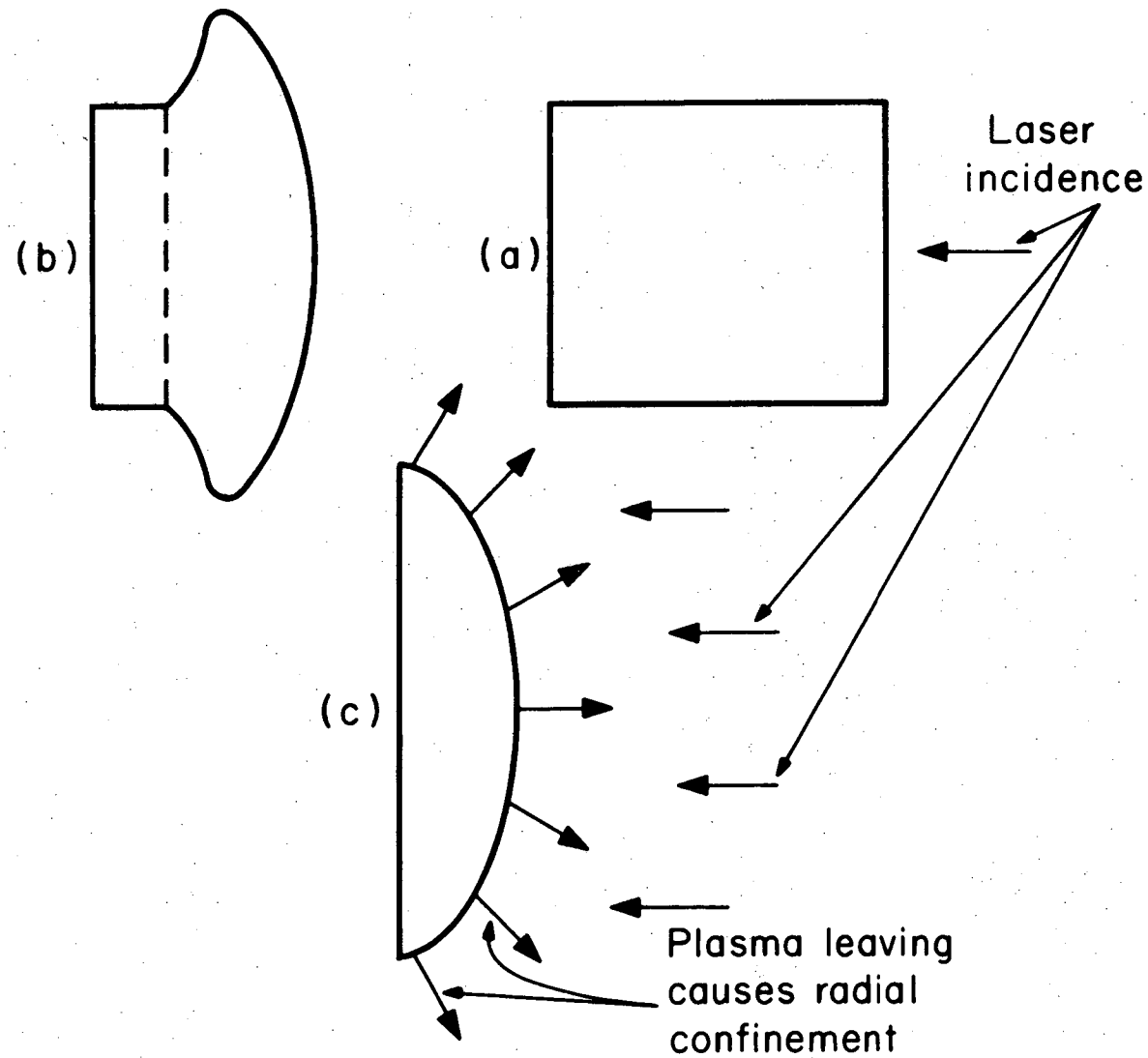

XBL749-4204

Fig. 2

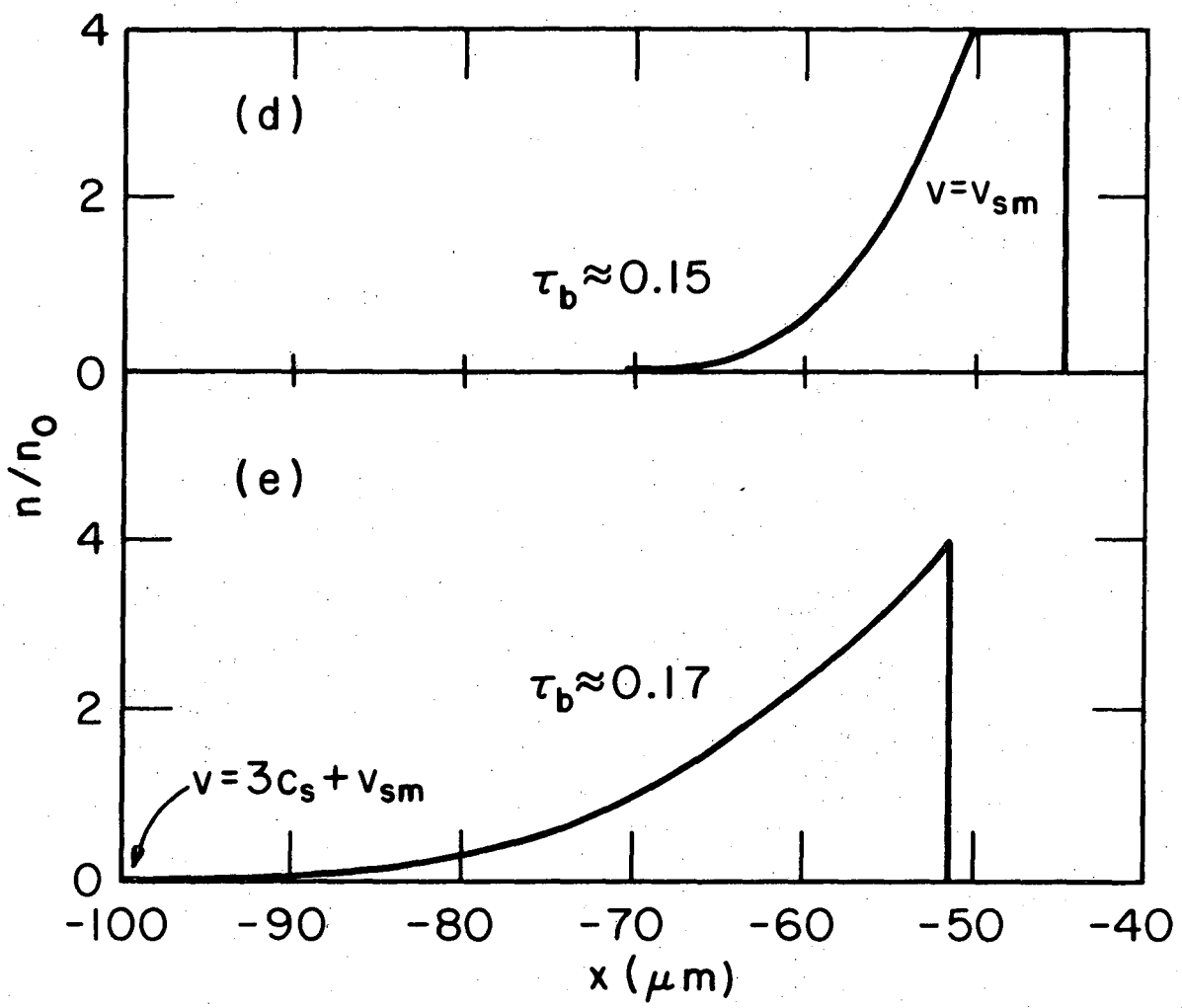

XBL 749-4201

Fig. 3

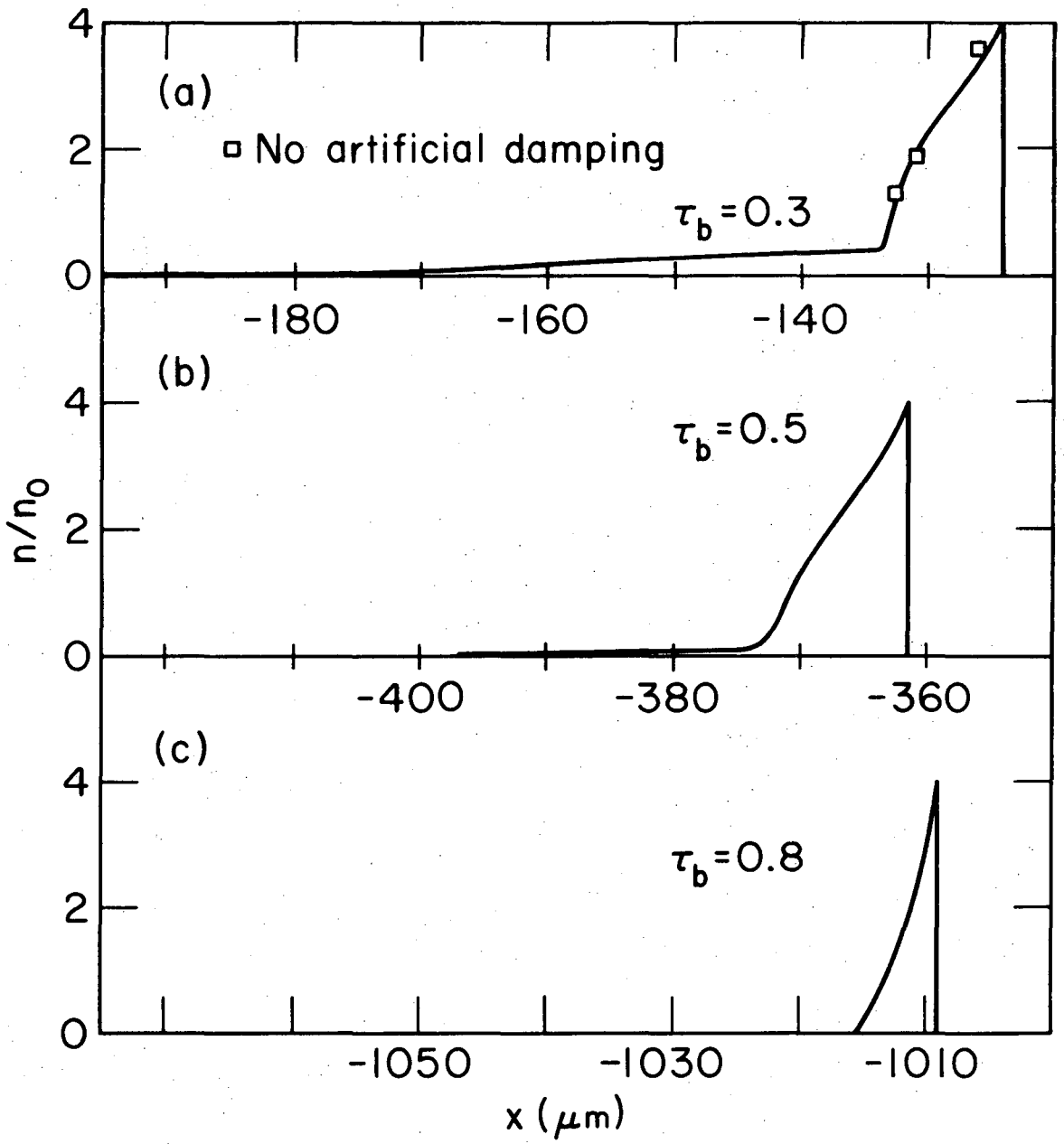
(a)
No artificial damping
$\tau_b = 0.3$
(b)
$\tau_b = 0.5$
(c)
$\tau_b = 0.8$
n/n_0
x (μm)
XBL 749-4199

Fig. 4

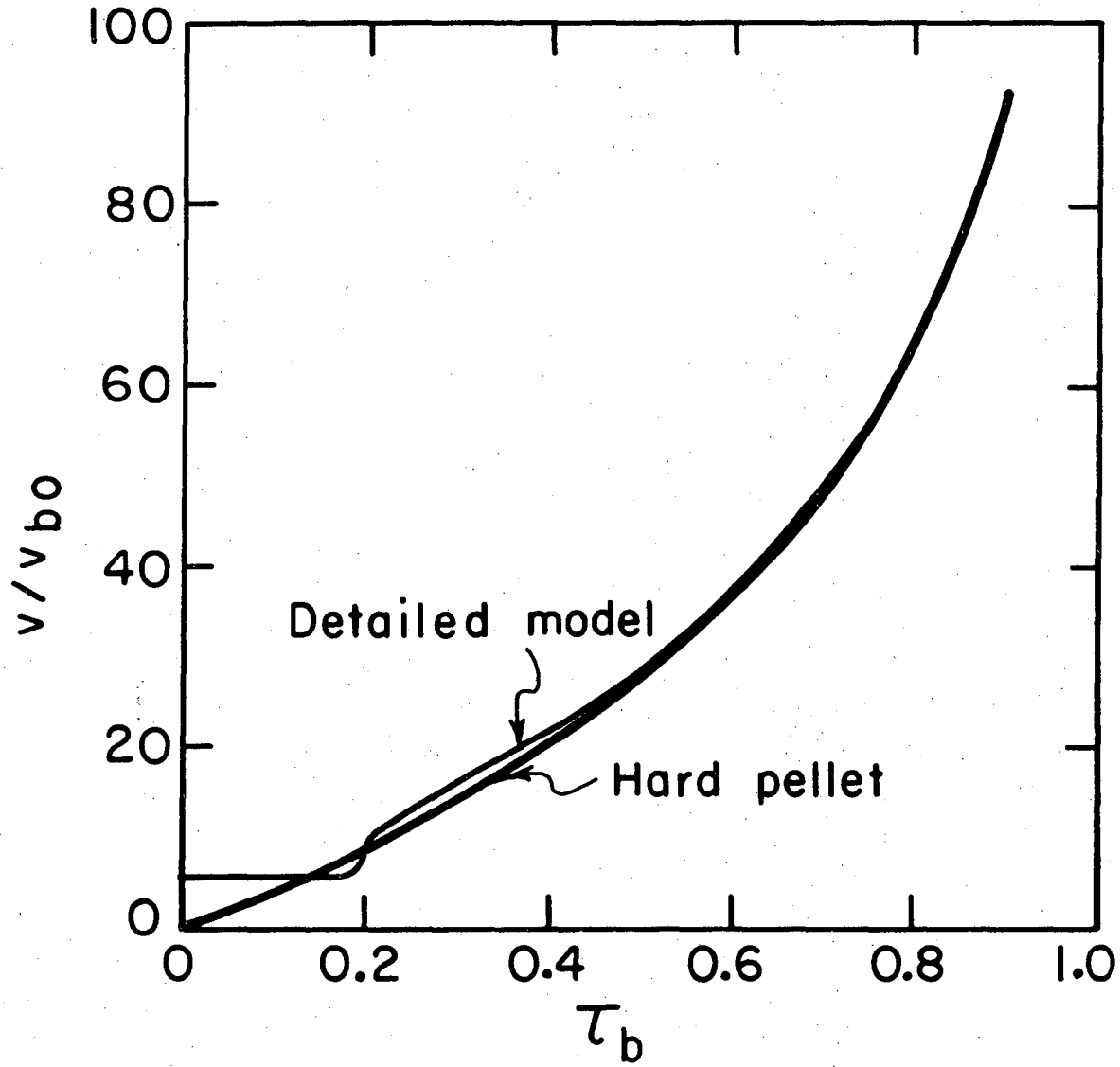

XBL748-3853

Fig. 5

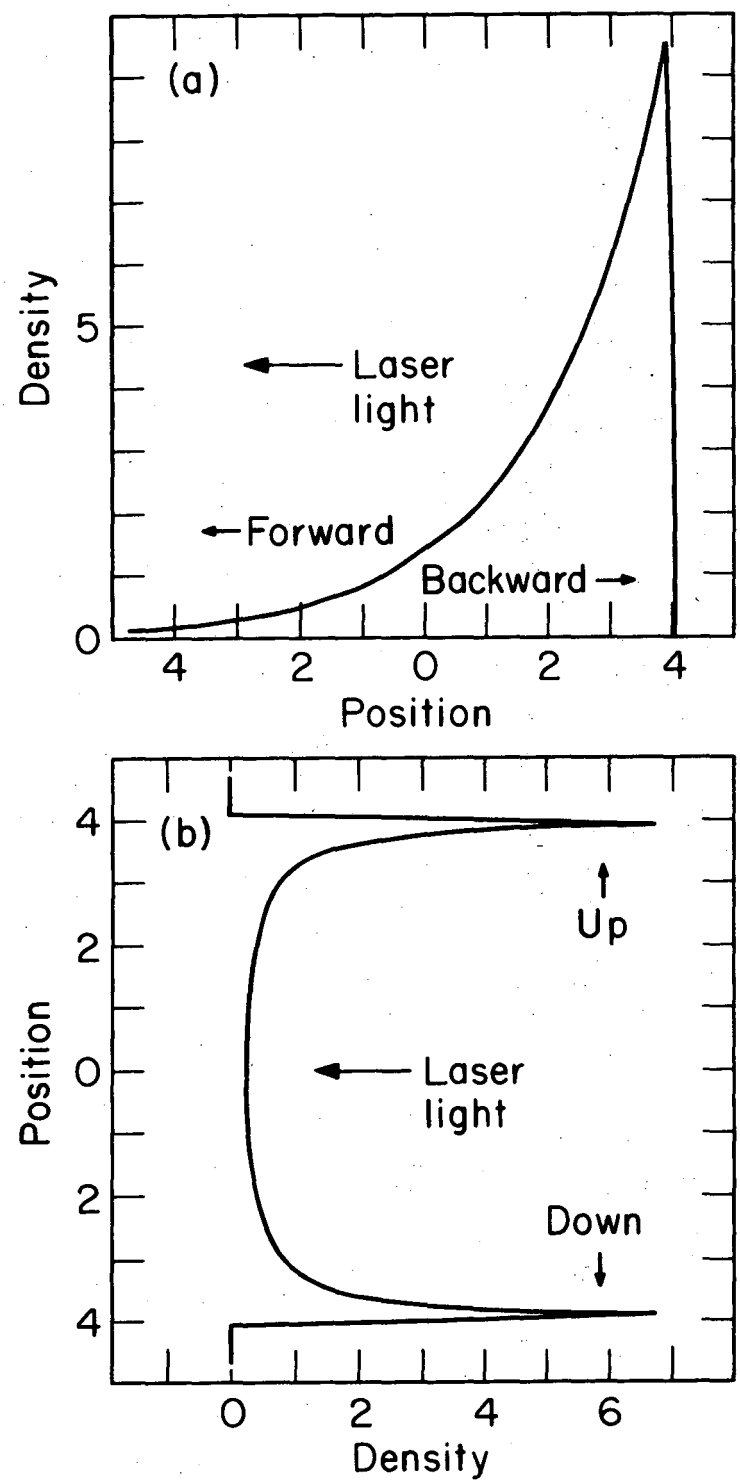

XBL749-4203

Fig. 6 (a) and (b)

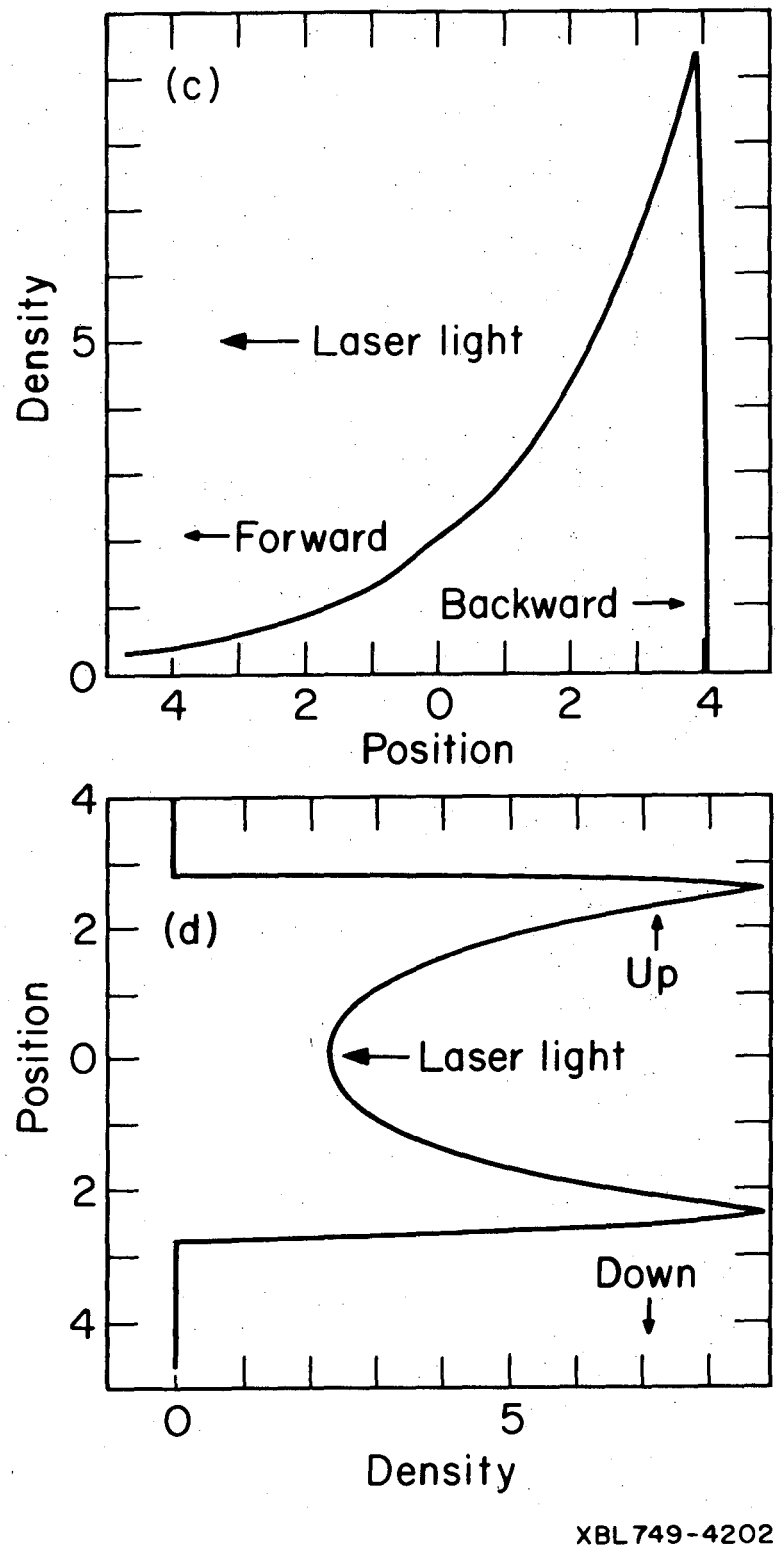
(c)
Density
5
0
Laser light
Forward
Backward
4
2
0
2
4
Position
(d)
Position
4
2
0
2
4
Up
Laser light
Down
0
5
Density
XBL749-4202

Fig. 6 (c) and (d)

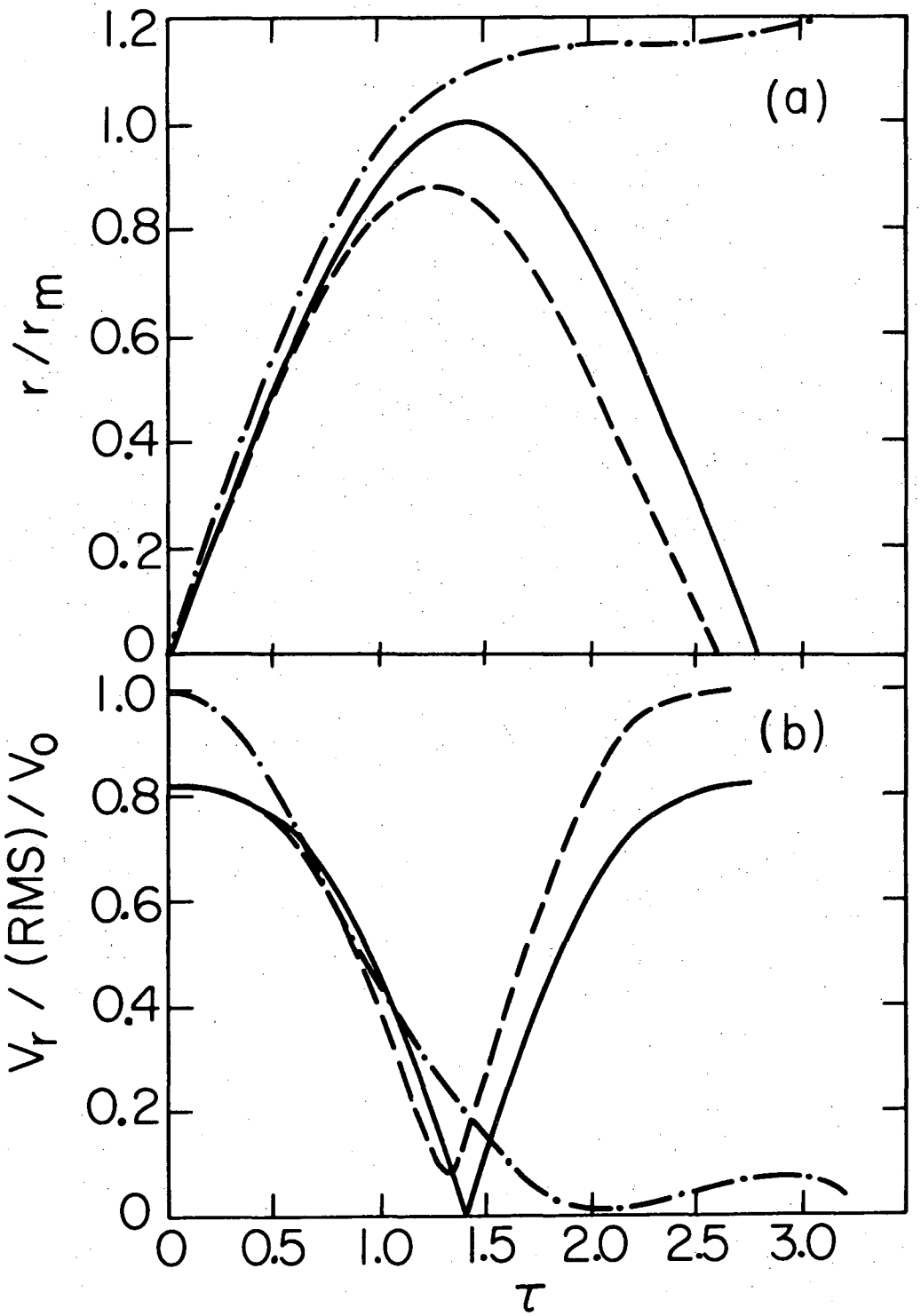

XBL748-3858

Fig. 7 (a) and (b)

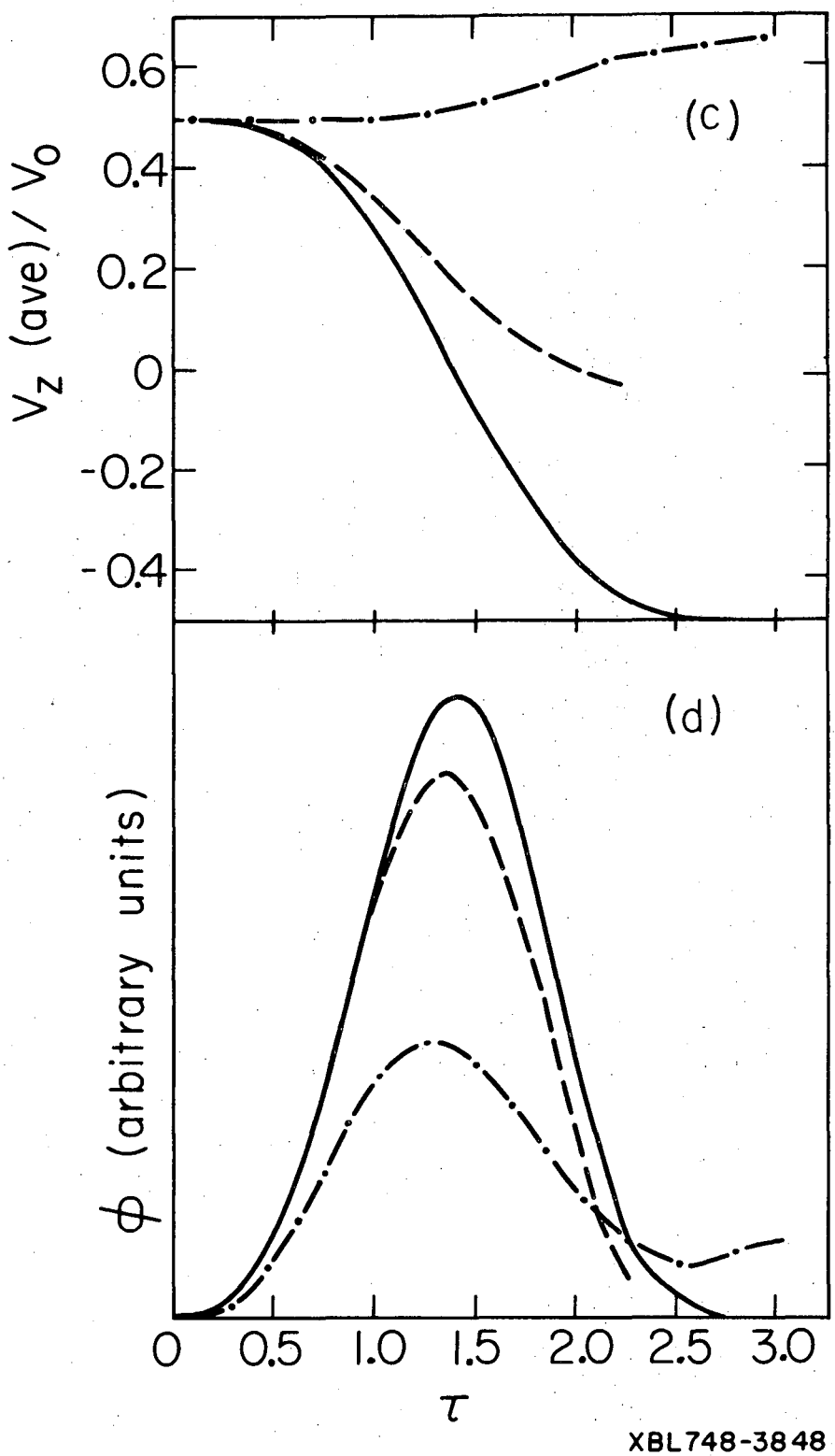
0.6
0.4
0.2
0
-0.2
-0.4
V_z (ave) / V_0
(c)
(d)
ϕ (arbitrary units)
0
0.5
1.0
1.5
2.0
2.5
3.0
τ
XBL748-3848

Fig. 7 (c) and (d)

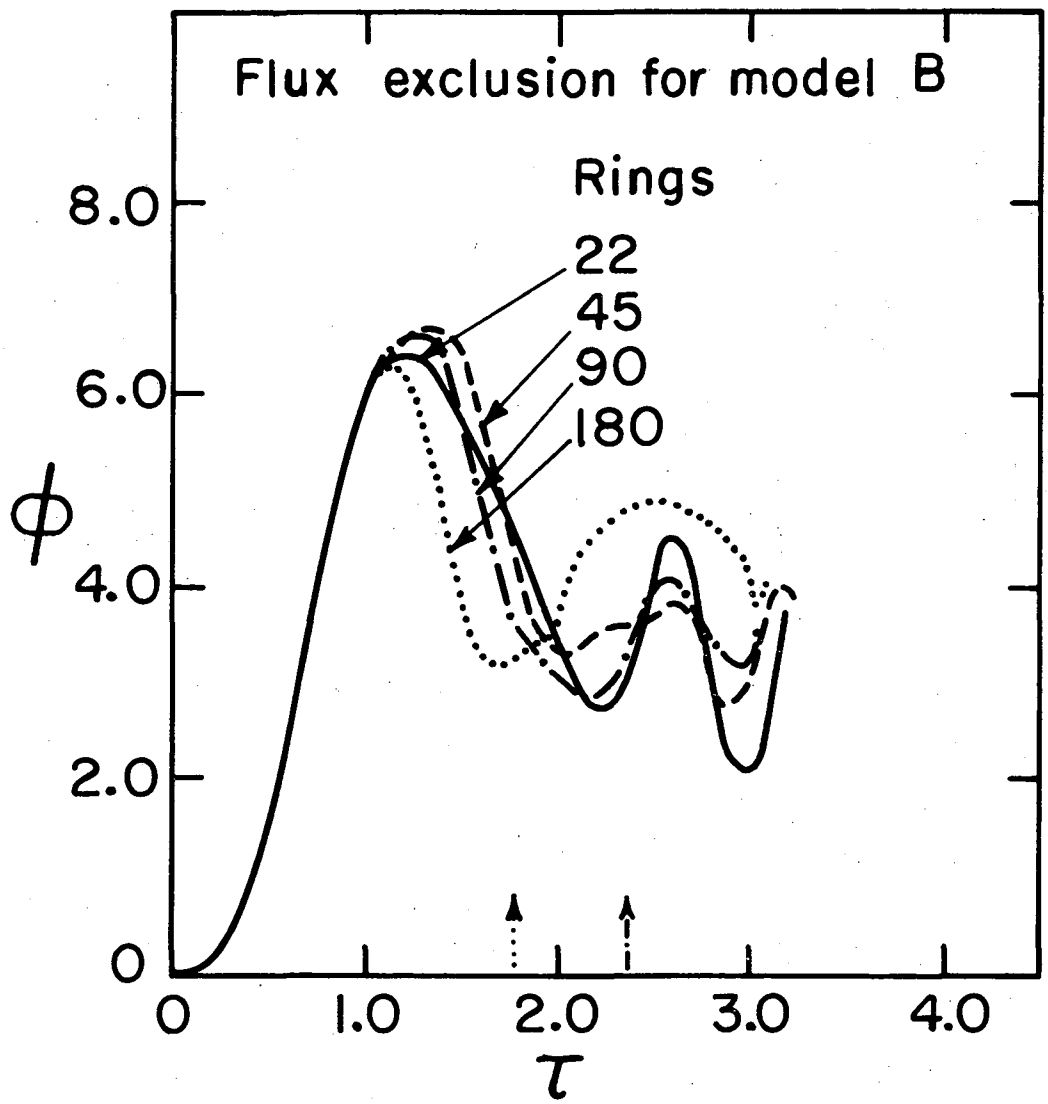

XBL748-3854

Fig.8

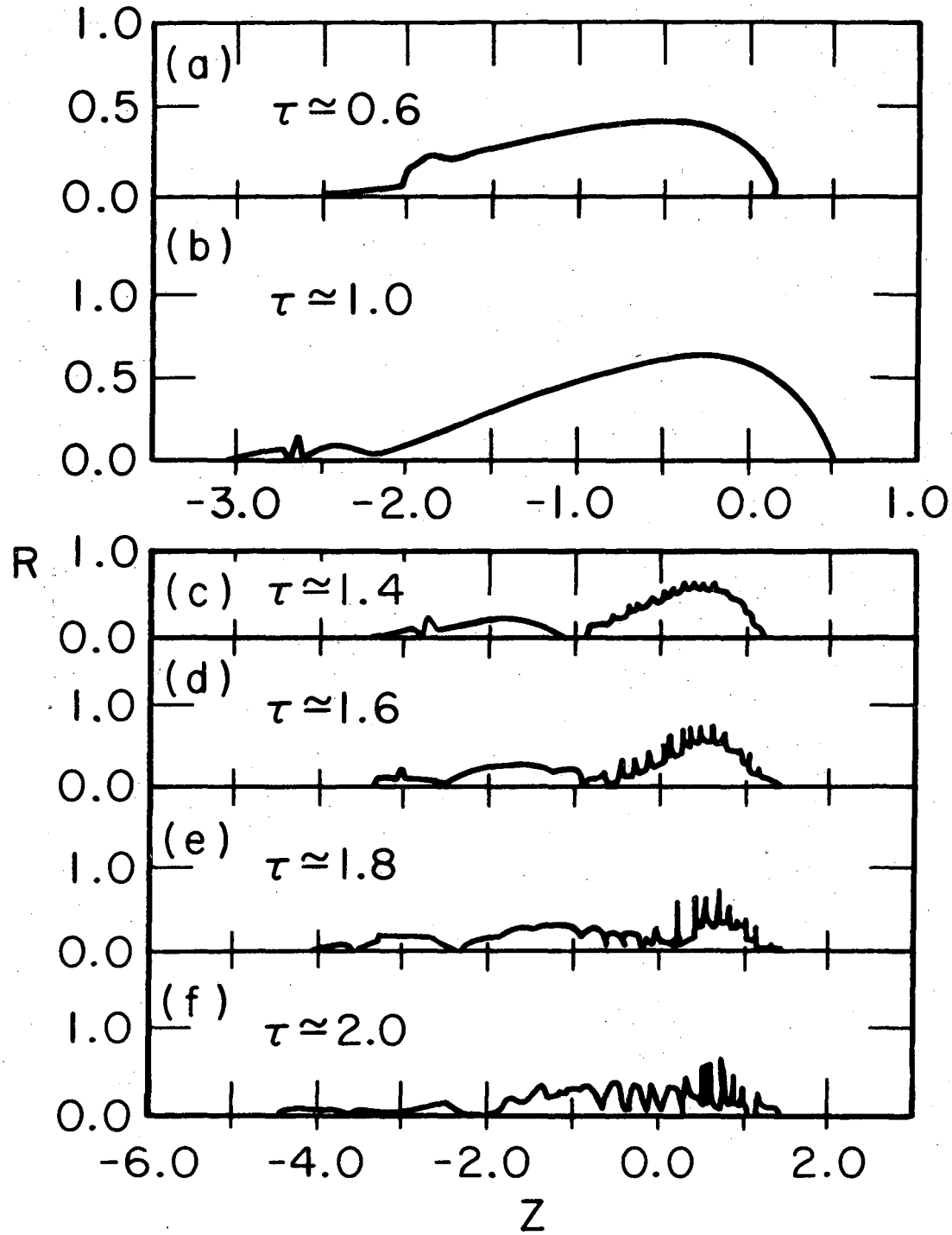

XBL 749-4205

Fig. 9

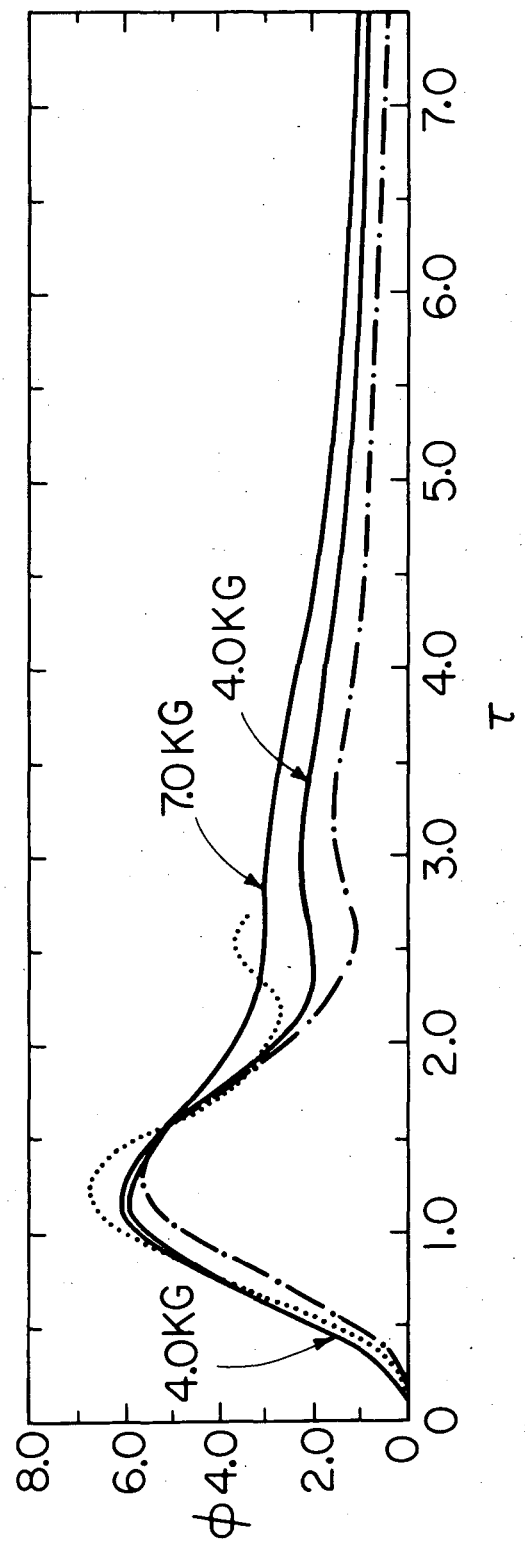

XBL748-3846

Fig. 10

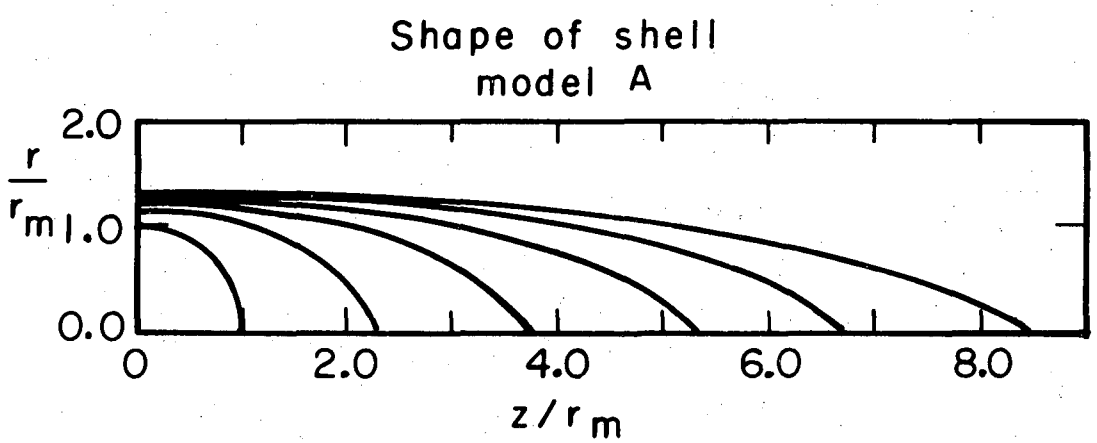

XBL748-3852

Fig. 11

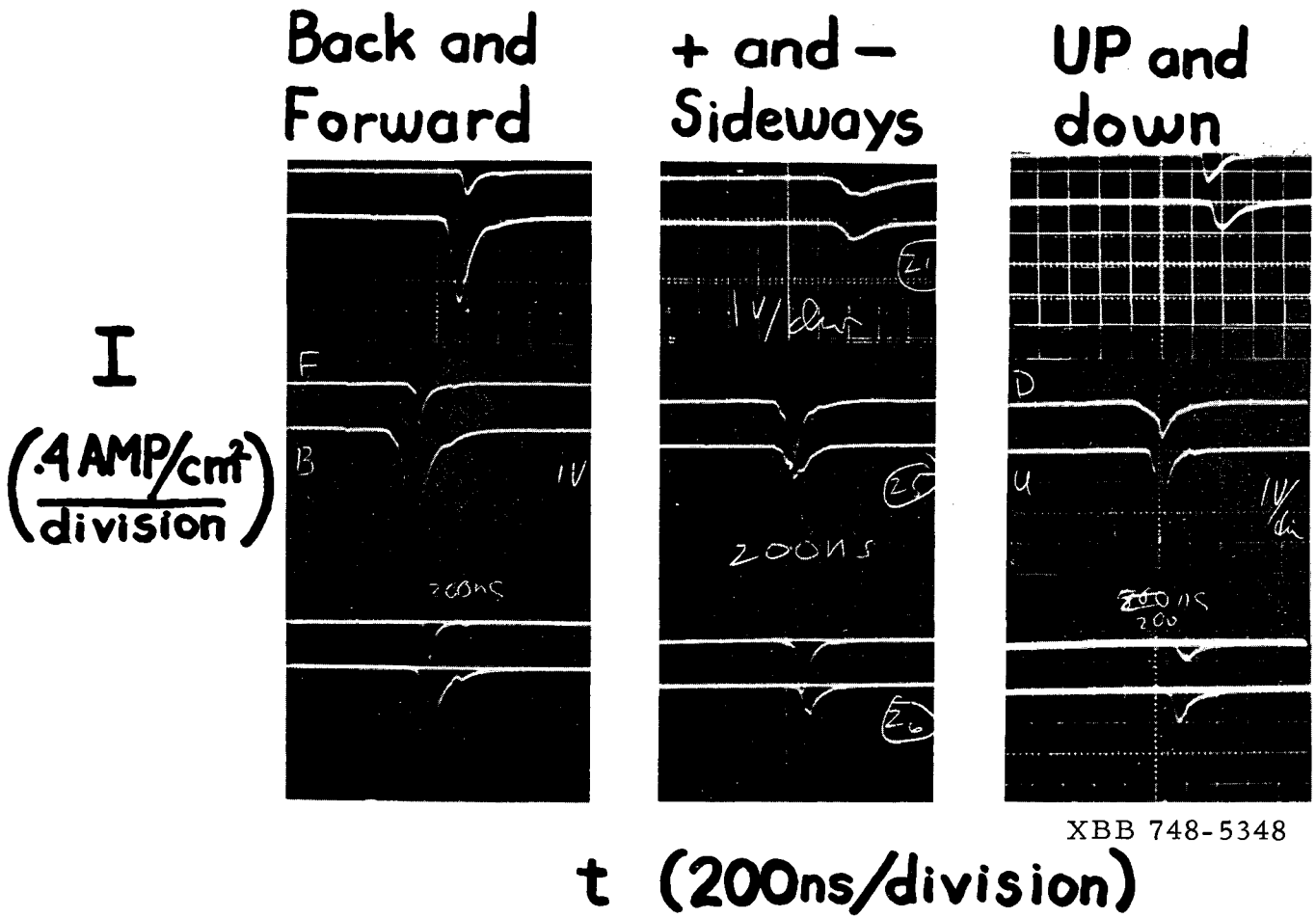

XBB 748-5348

Fig. 12

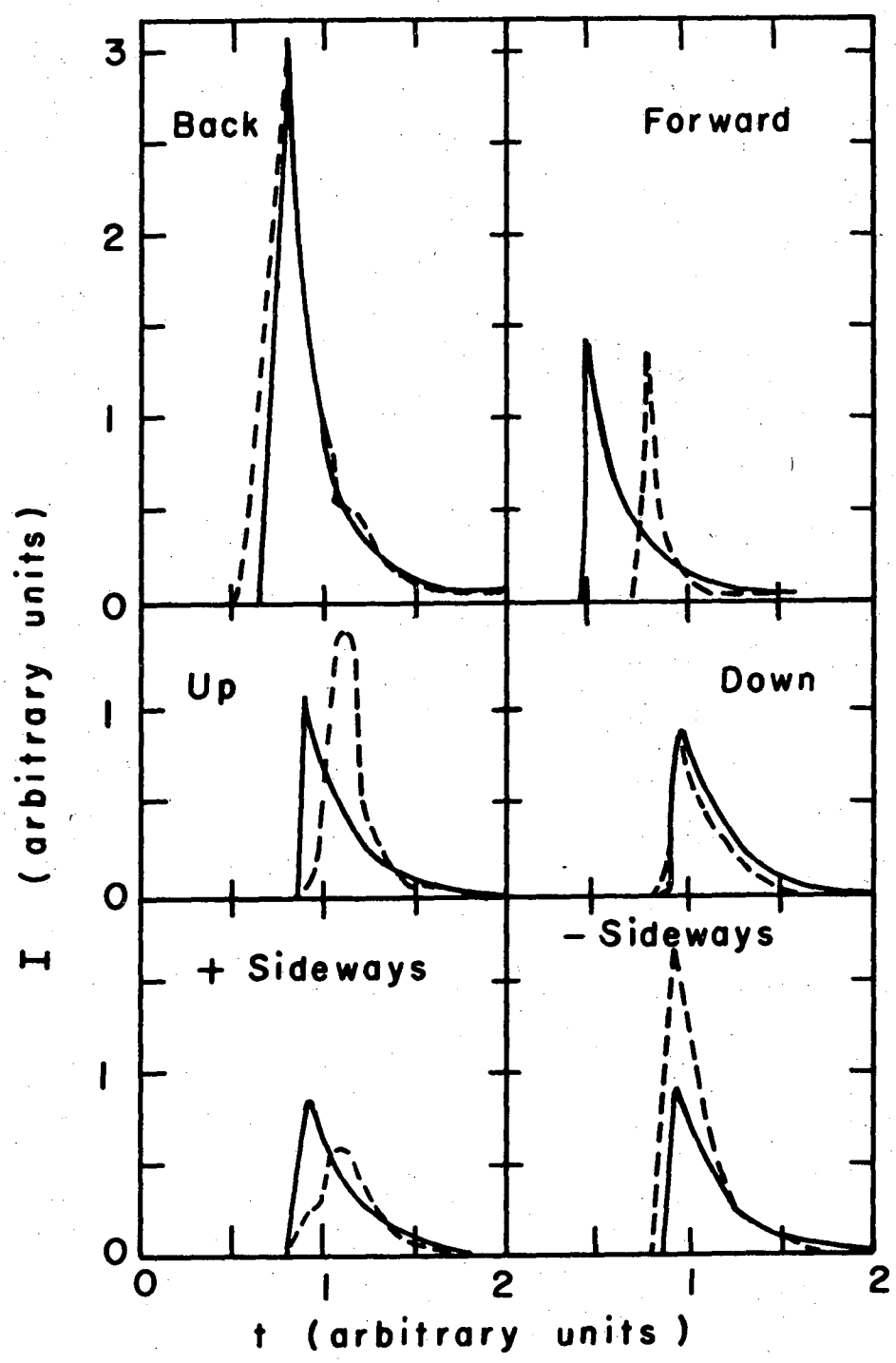

XBL 748-3847

Fig. 13

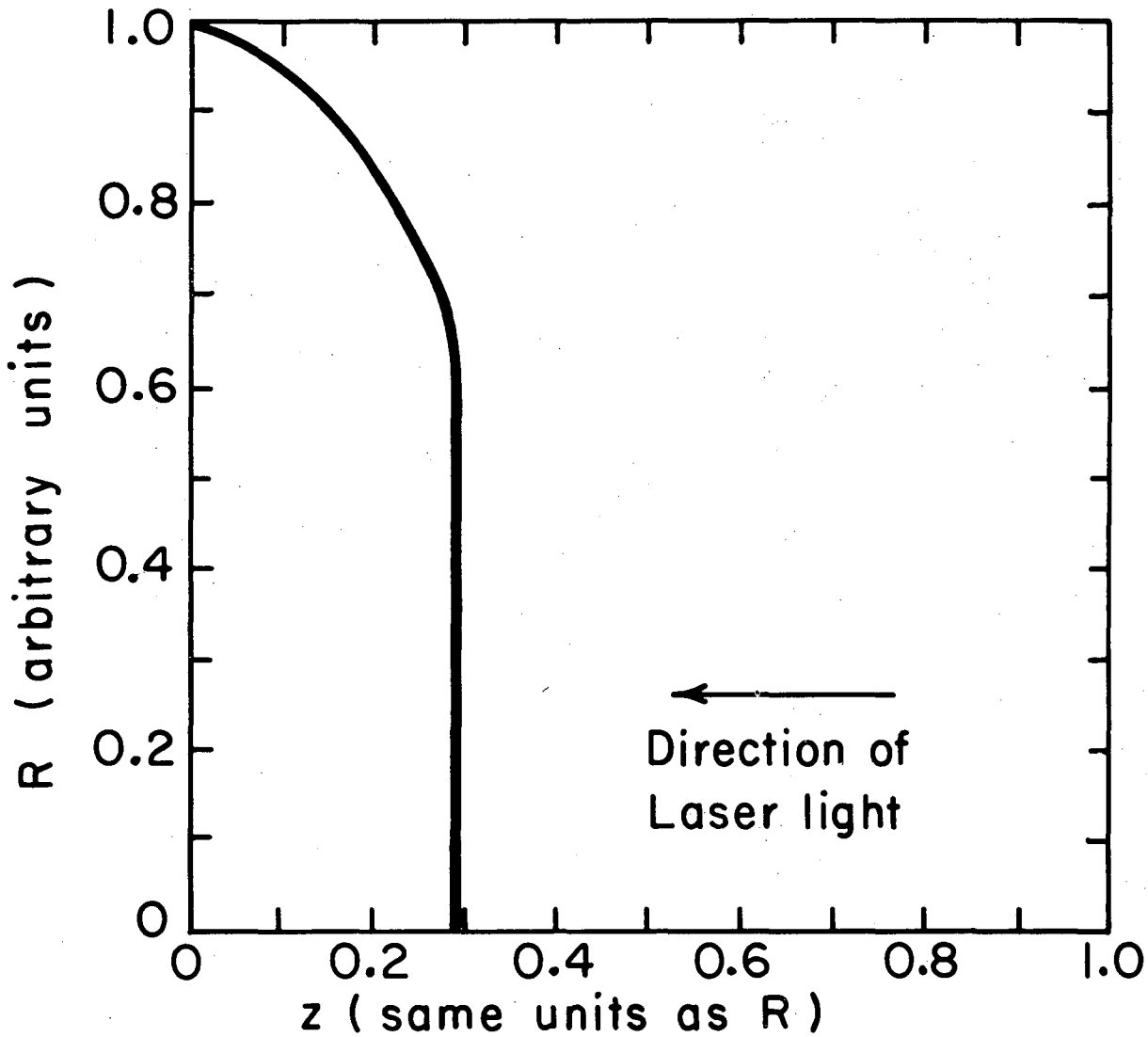

XBL748- 3851

Fig. 14

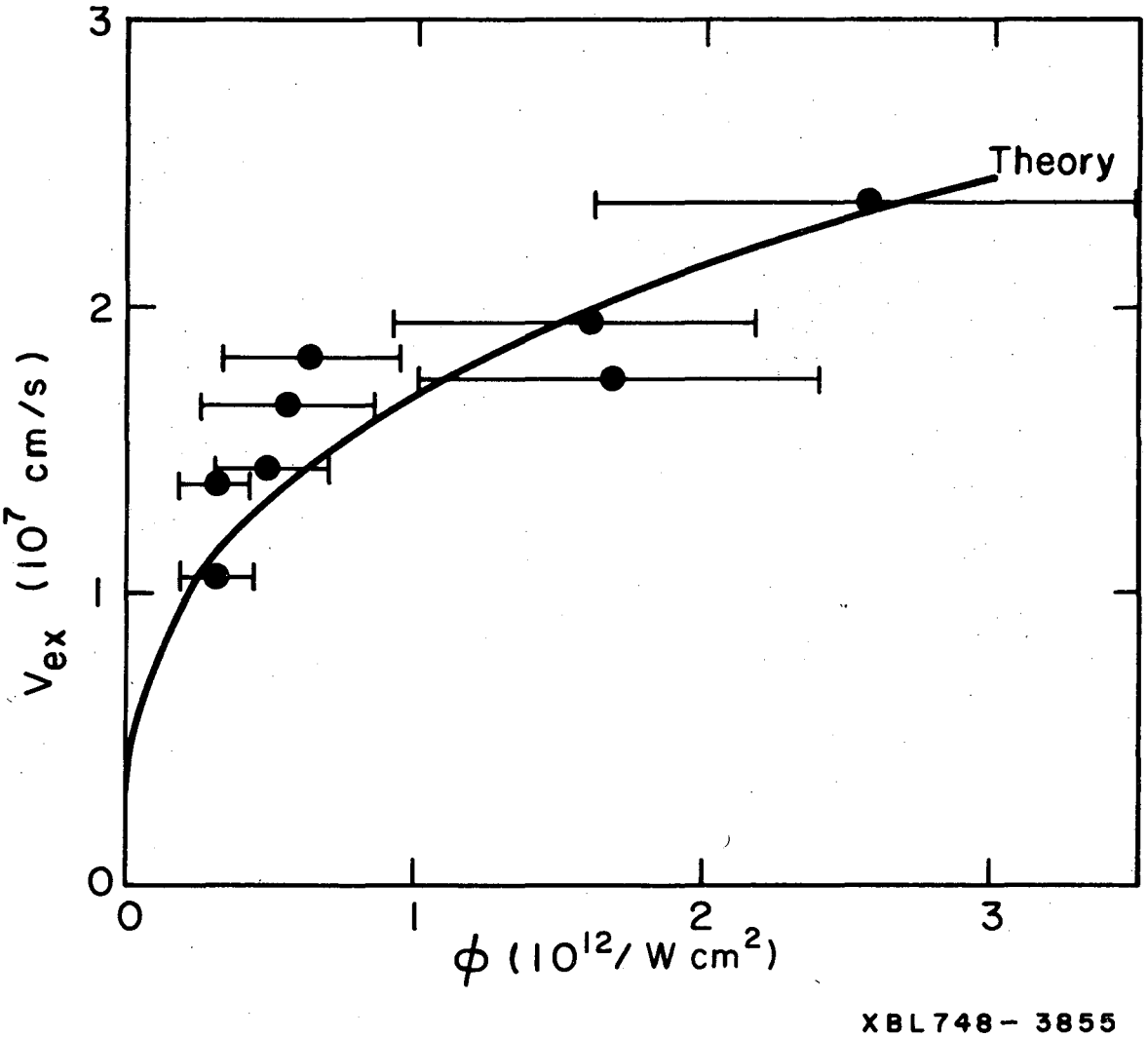

Fig. 15

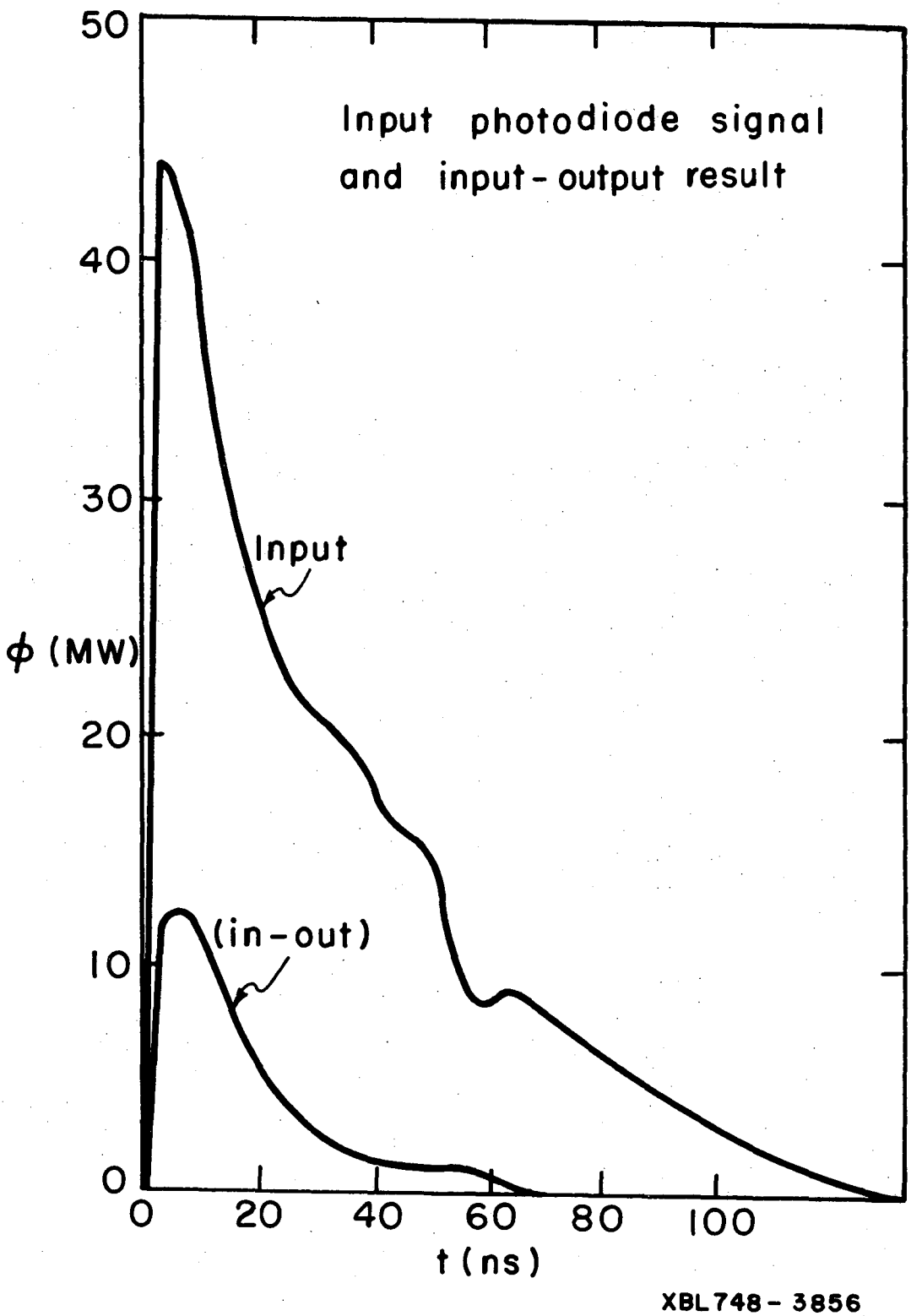
Input photodiode signal
and input-output result
Input
(in-out)
φ (MW)
t (ns)
0
10
20
30
40
50
0
20
40
60
80
100
XBL748-3856

Fig. 16

0 0 0 0 4 1 0 8 1 6 6

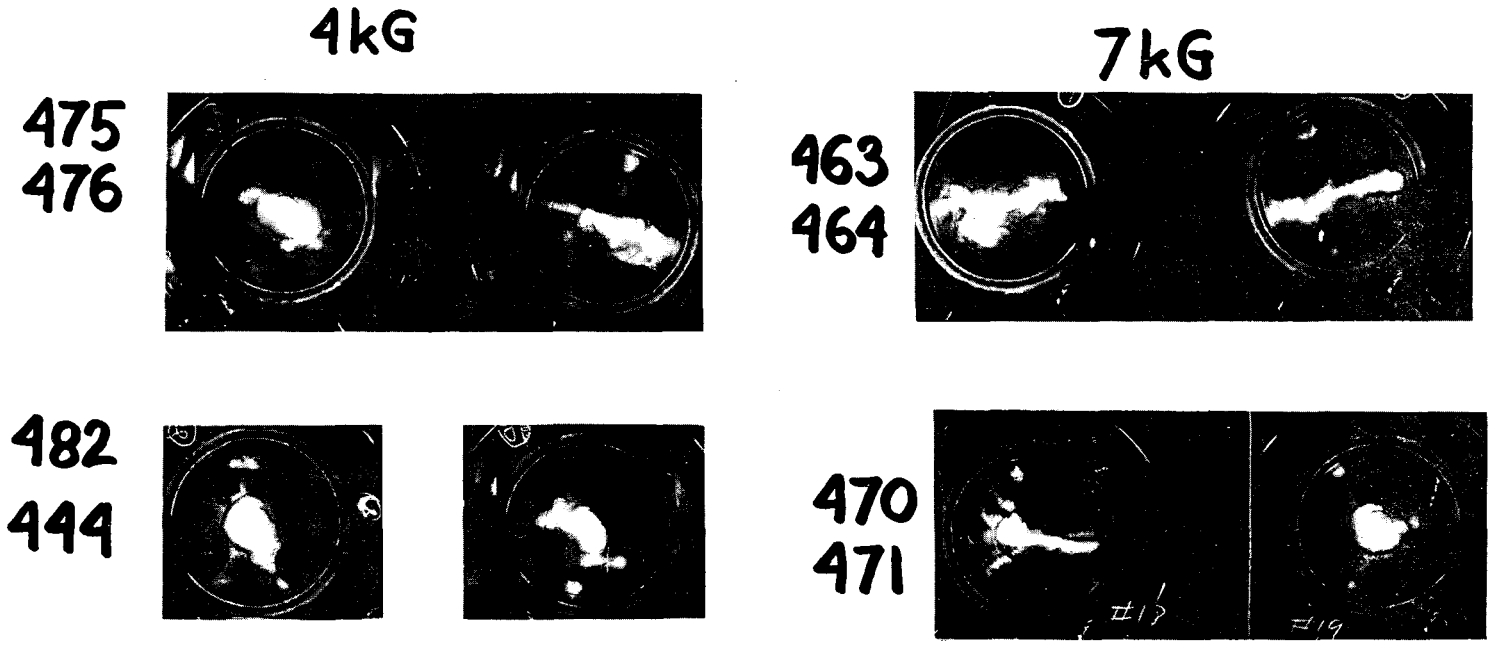

XBB 748-5349

Fig. 17

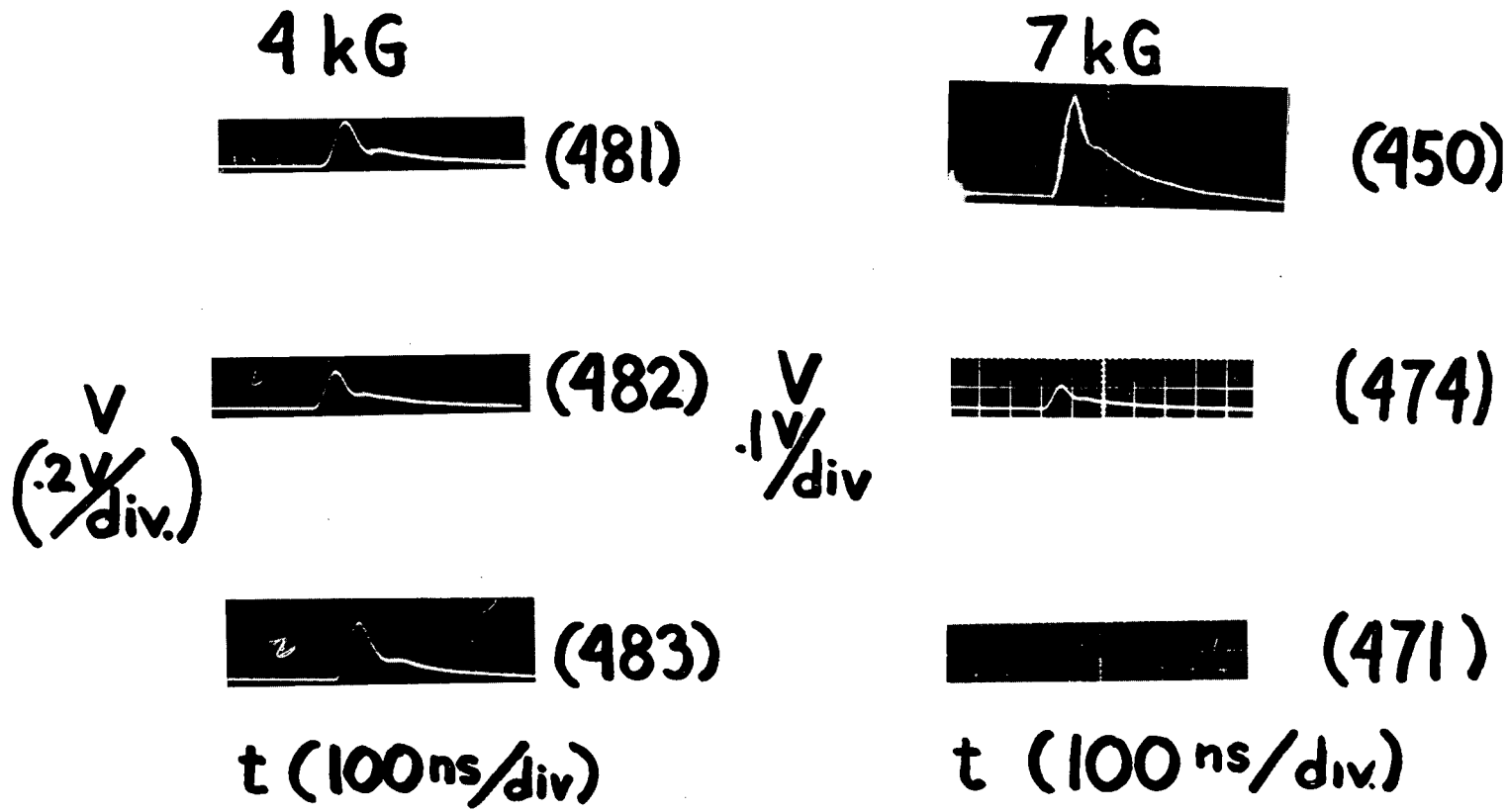

XBB 748-5350

Fig. 18

0 0 0 0 4 1 0 8 1 6 7

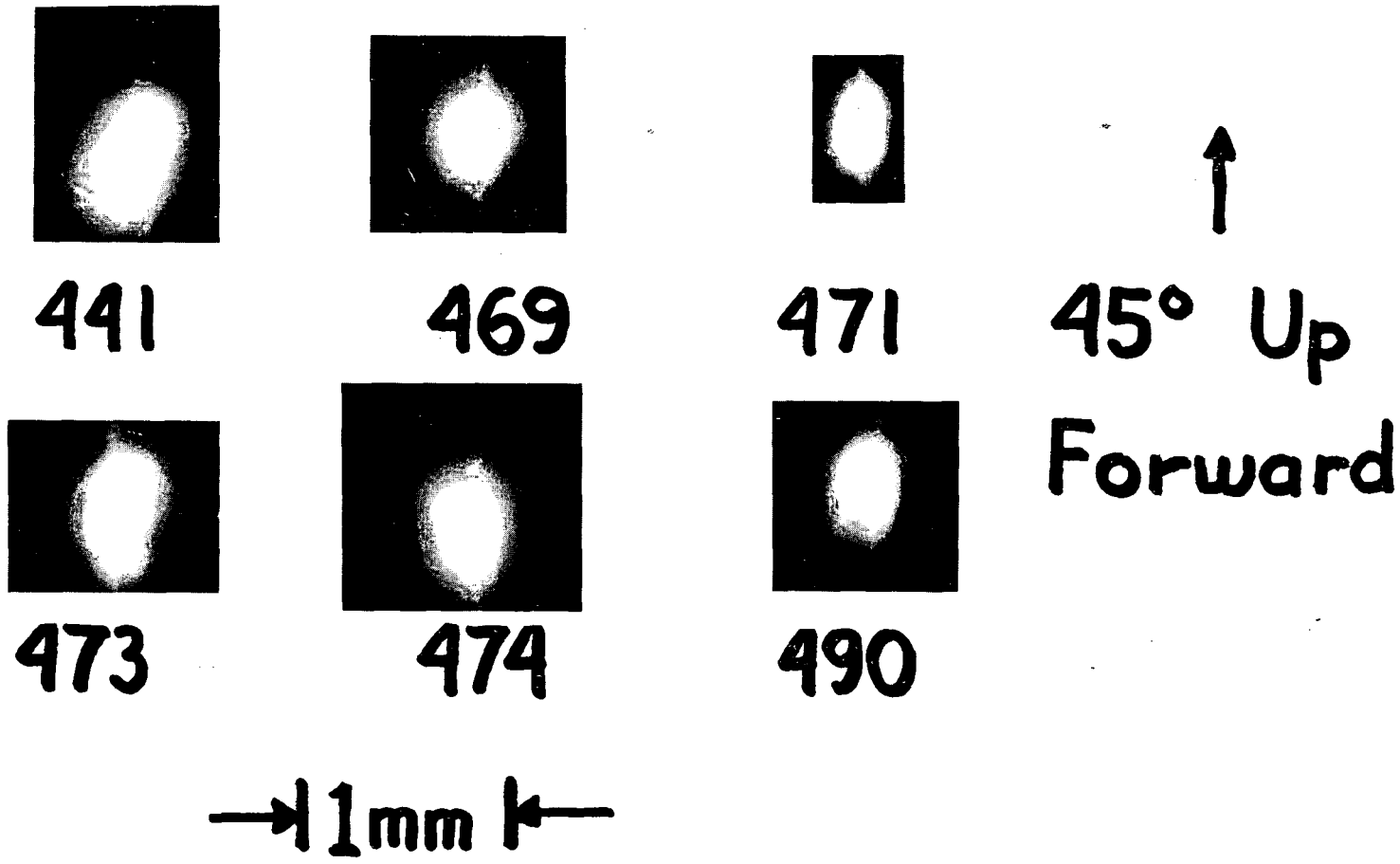

XBB 748-5351

Fig. 19

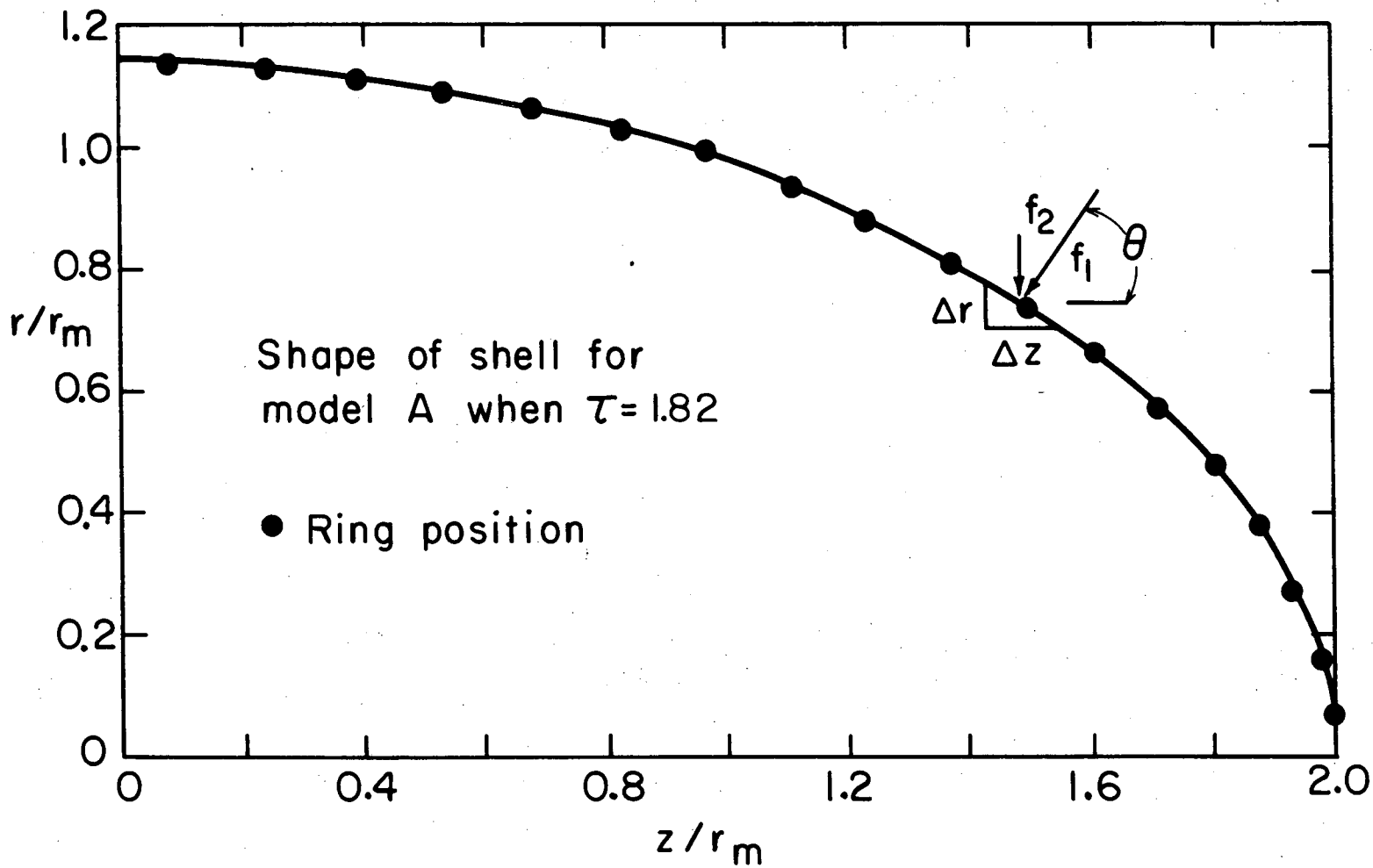

XBL748-3857

Fig. 20

0 0 0 0 4 1 6 8 1 6 8

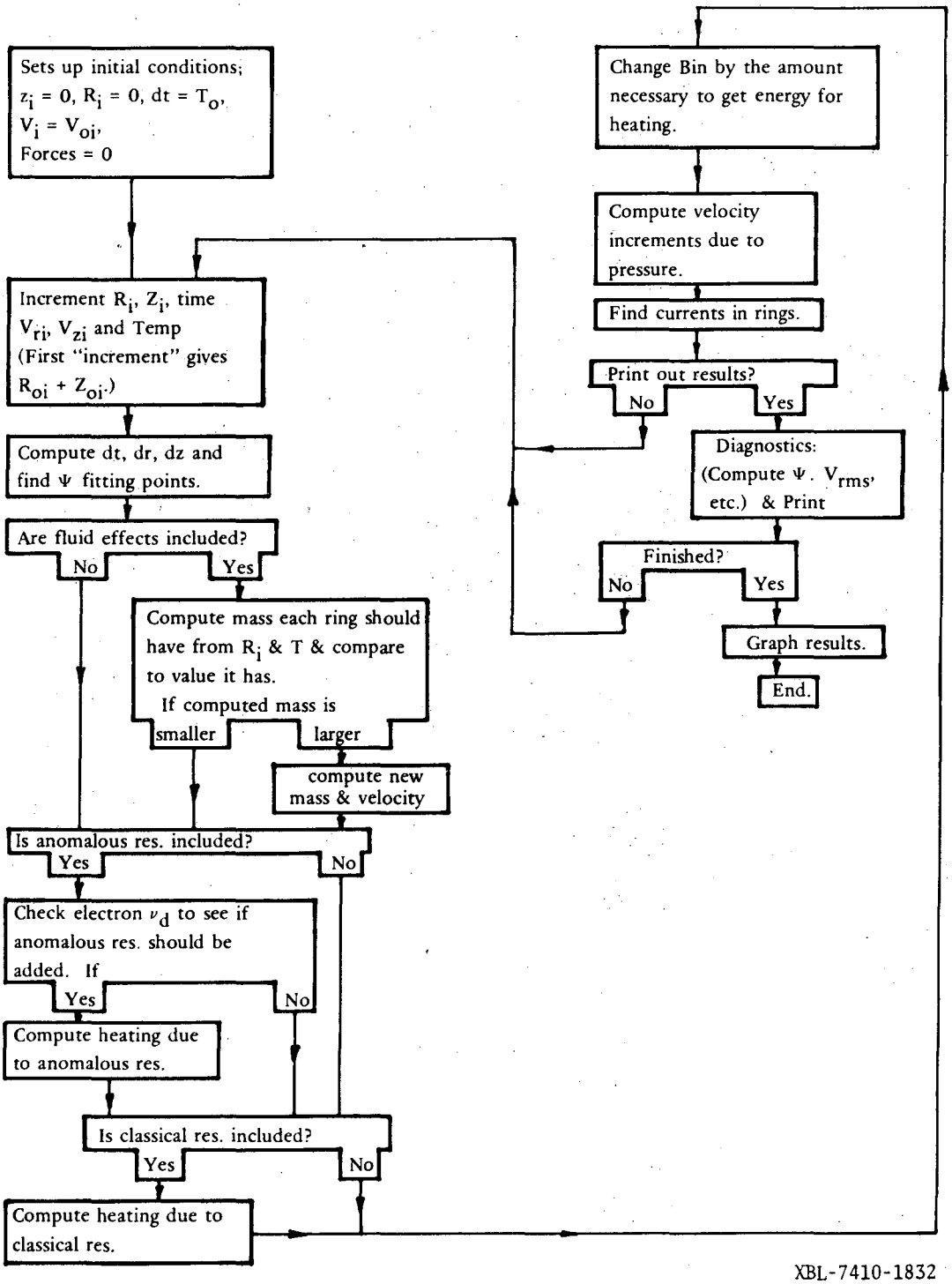

XBL-7410-1832

Fig. 21

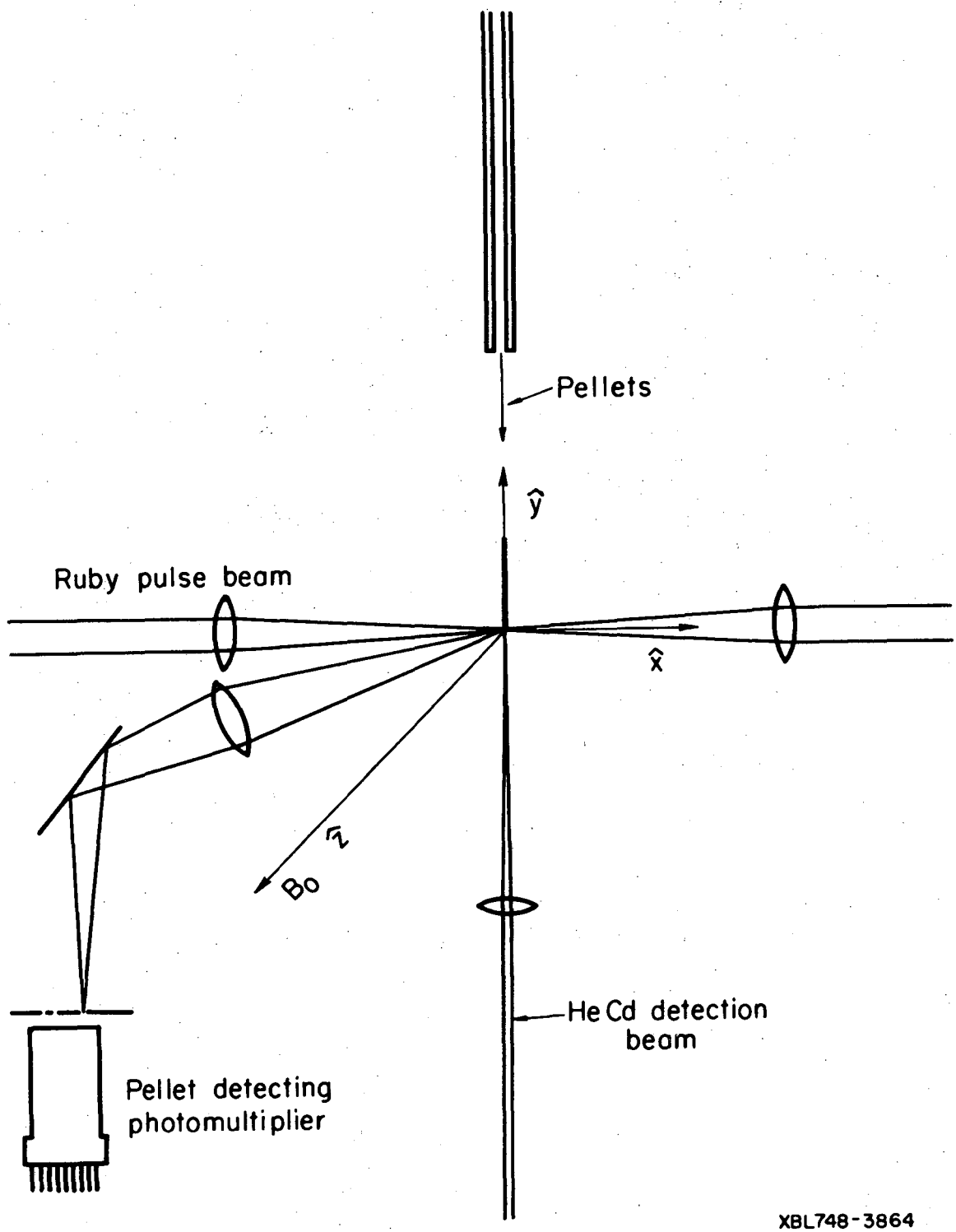
Pellets
ŷ
Ruby pulse beam
x̂
ẑ
Bo
He Cd detection beam
Pellet detecting photomultiplier
XBL748-3864

Fig. 22

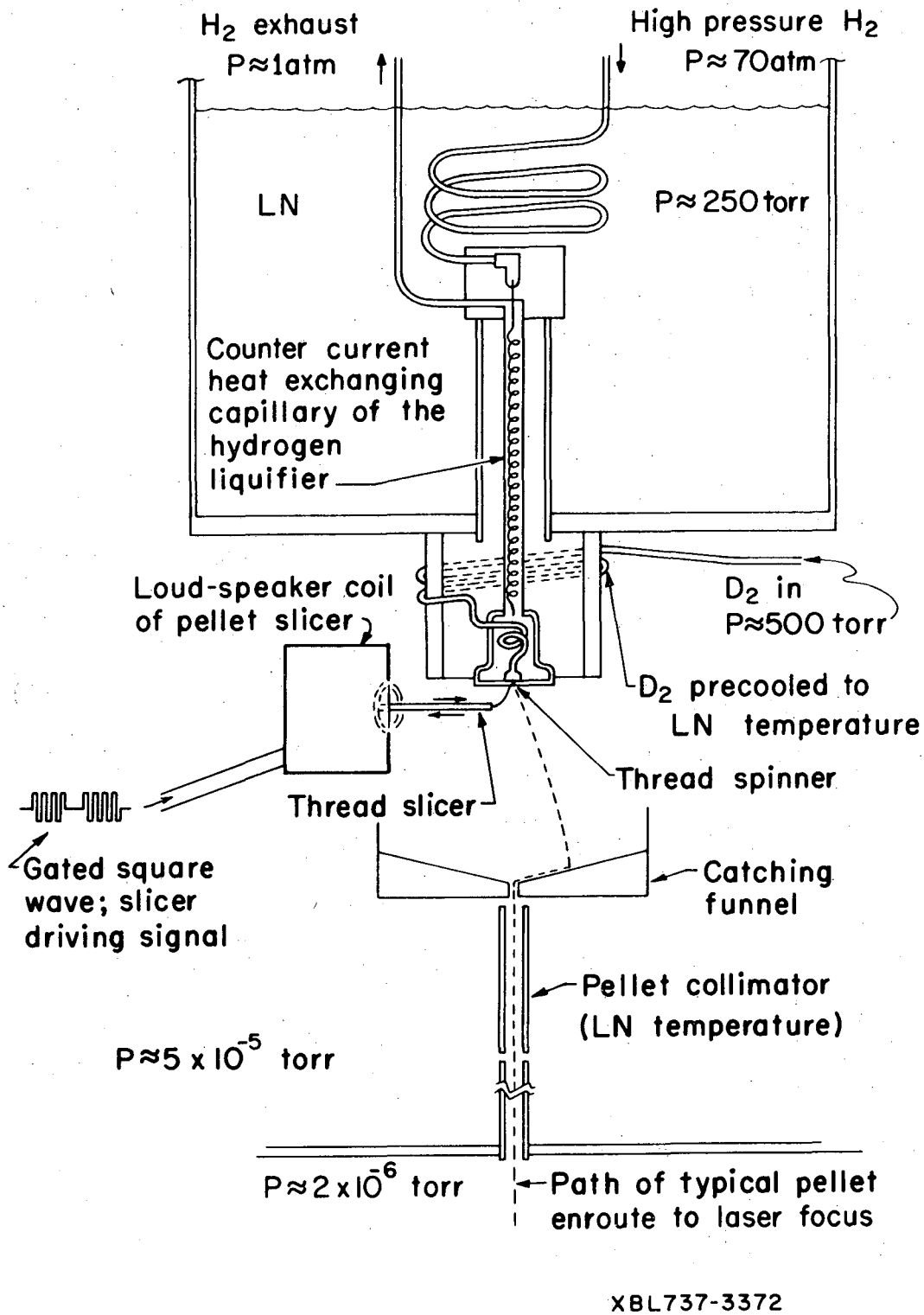

XBL737-3372

Fig. 23

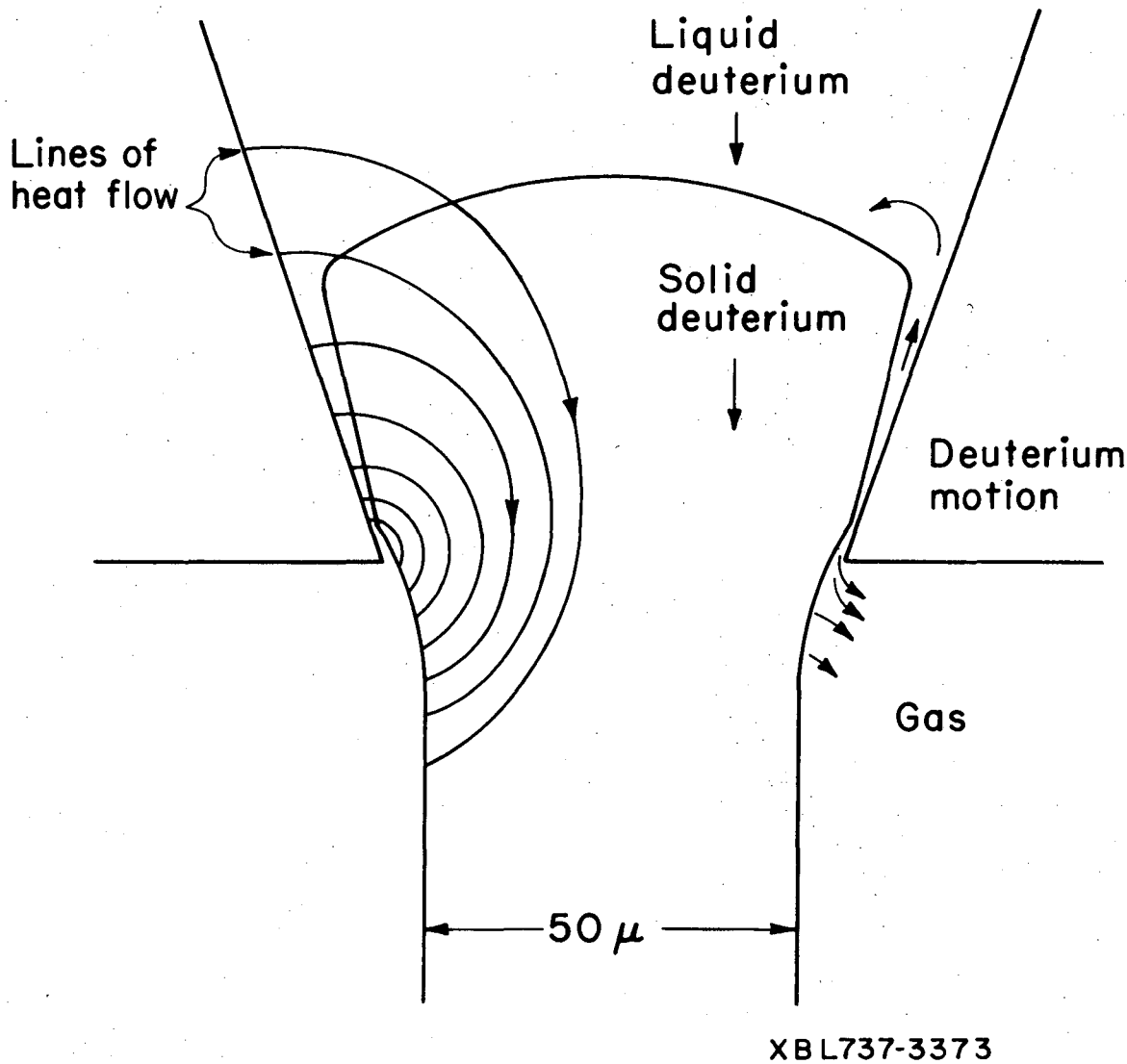
Liquid
deuterium
Lines of
heat flow
Solid
deuterium
Deuterium
motion
Gas
50 μ
XBL737-3373

Fig. 24

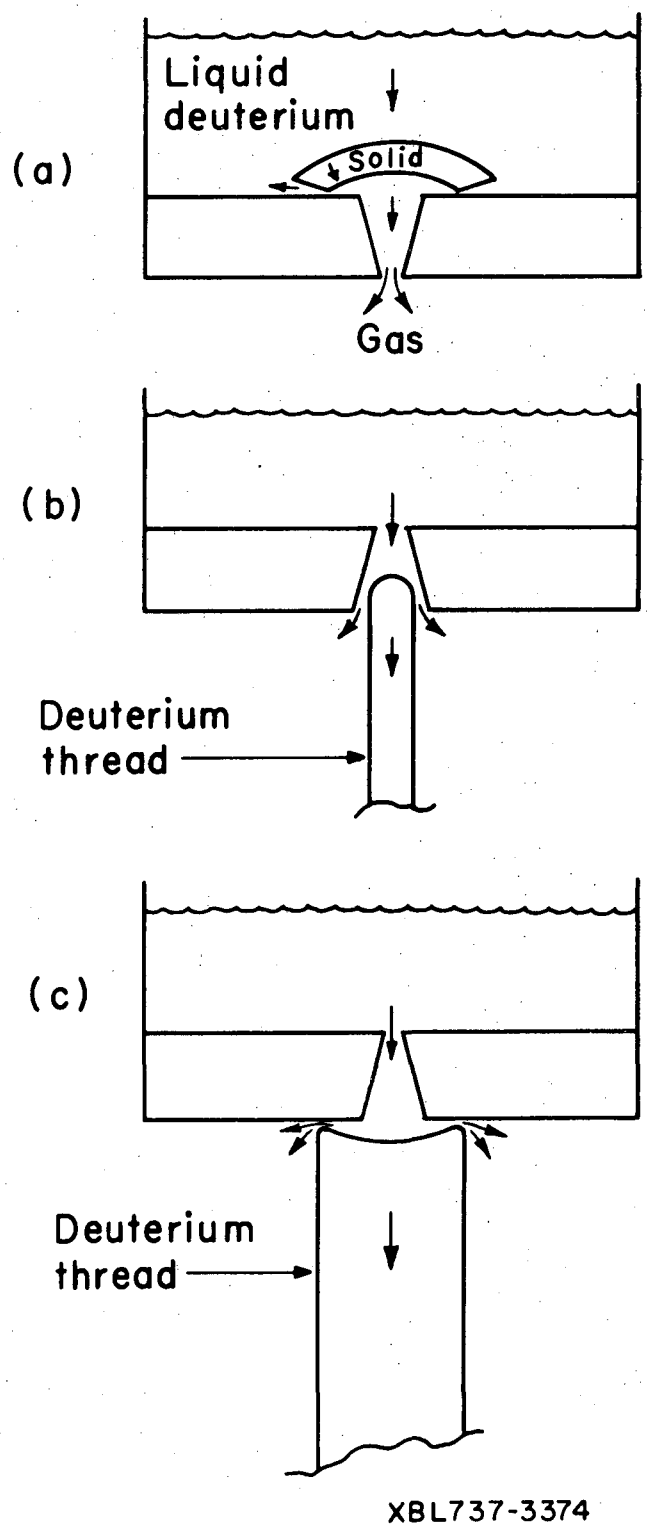
(a)
Liquid deuterium
Solid
Gas
(b)
Deuterium thread
(c)
Deuterium thread
XBL737-3374

Fig. 25

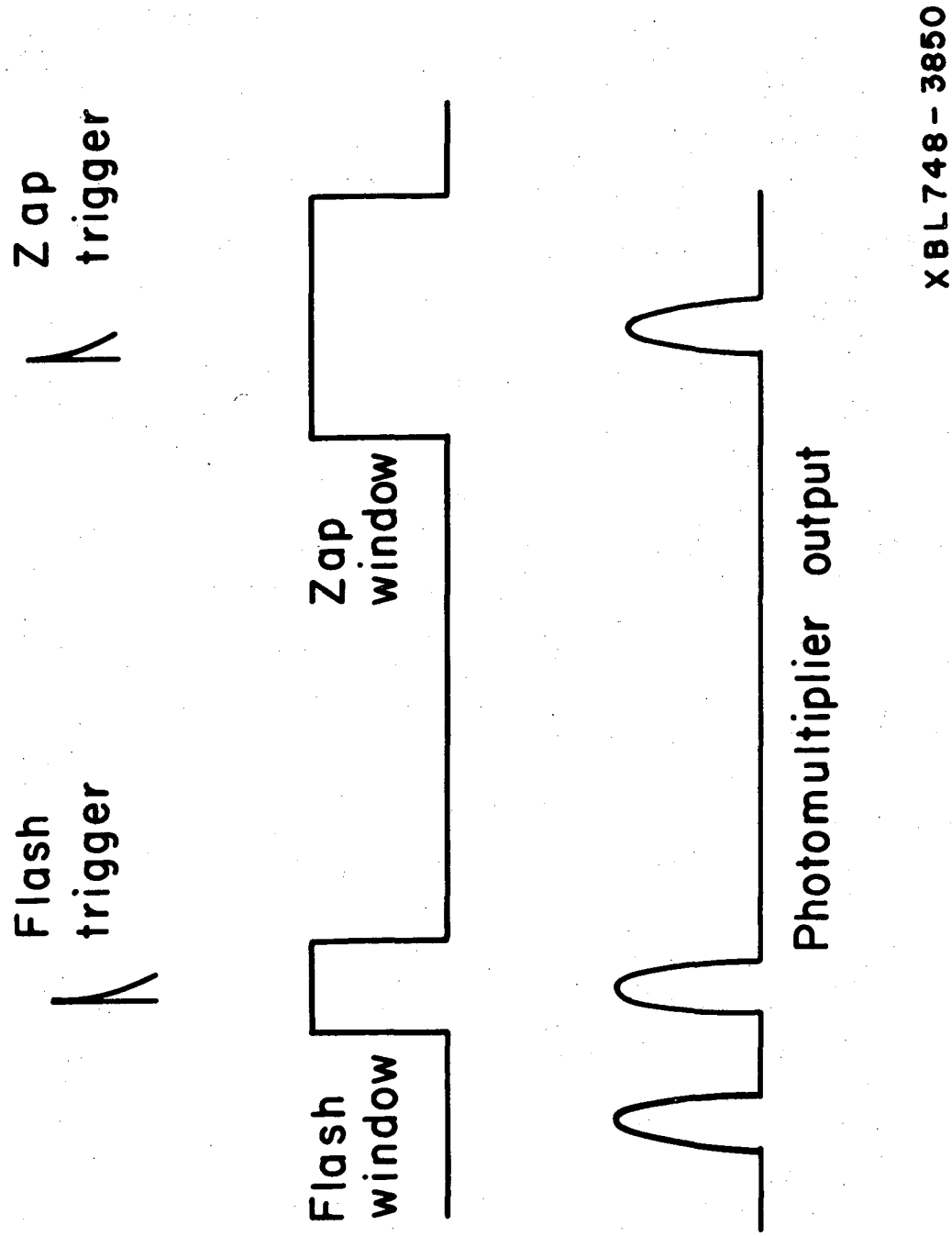
Flash trigger
Zap trigger
Flash window
Zap window
Photomultiplier output
XBL748-3850

Fig. 26

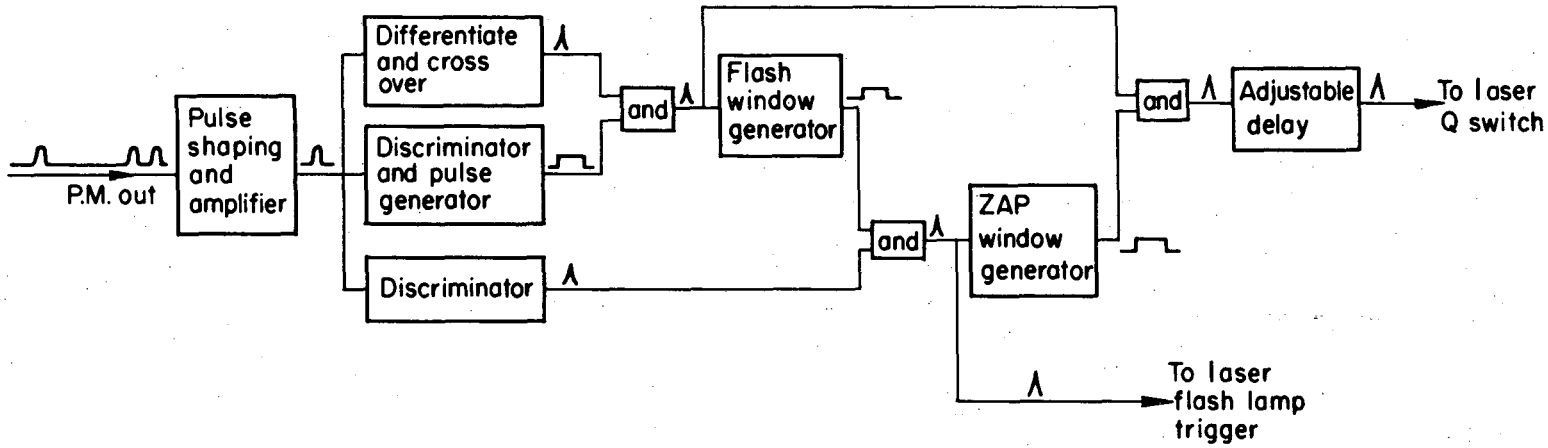

XBL748-3863

Fig. 27

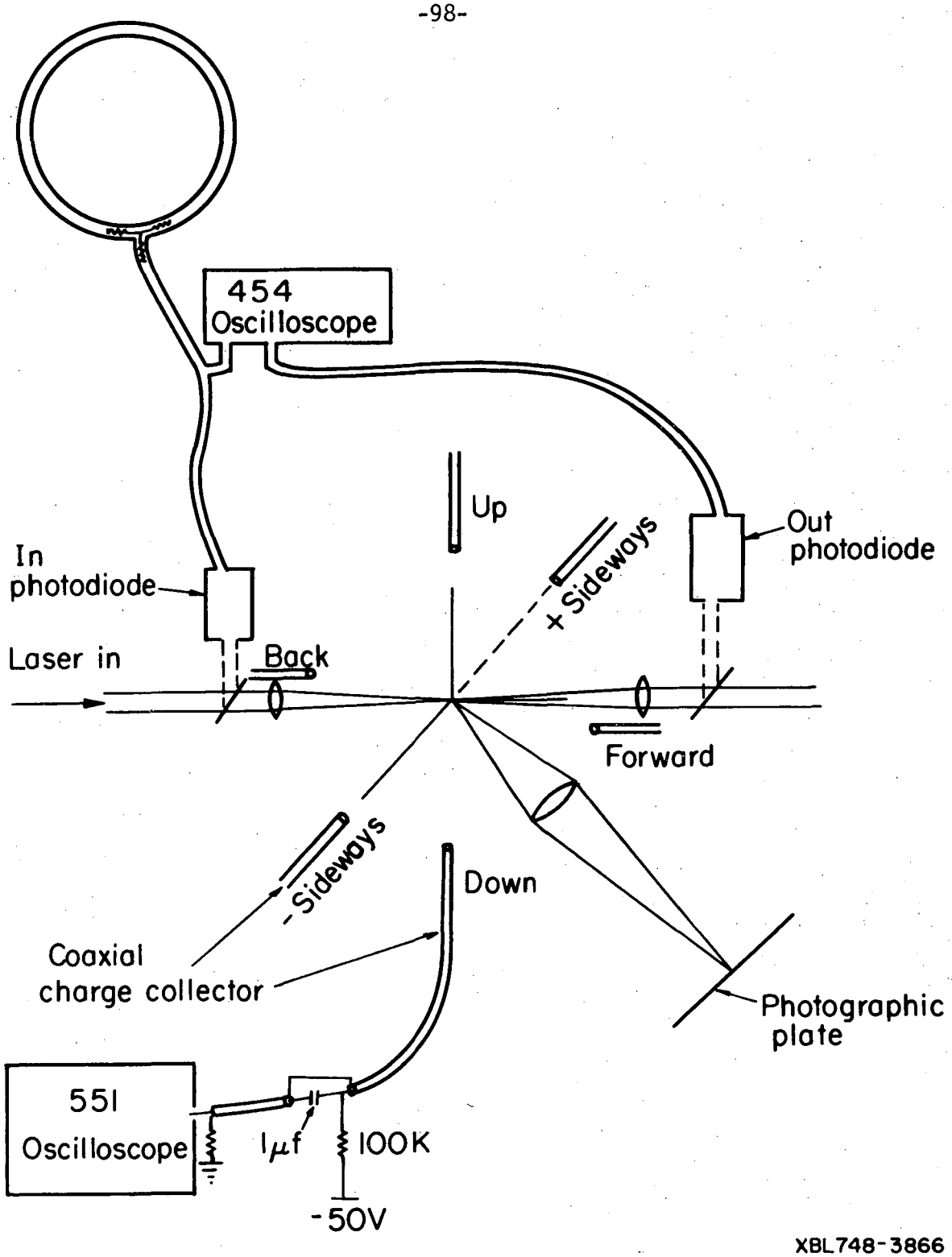
454
Oscilloscope
Up
+ Sideways
Out
photodiode
In
photodiode
Laser in
Back
Forward
- Sideways
Down
Coaxial
charge collector
Photographic
plate
551
Oscilloscope
1μf
100K
-50V
XBL748-3866

Fig. 28

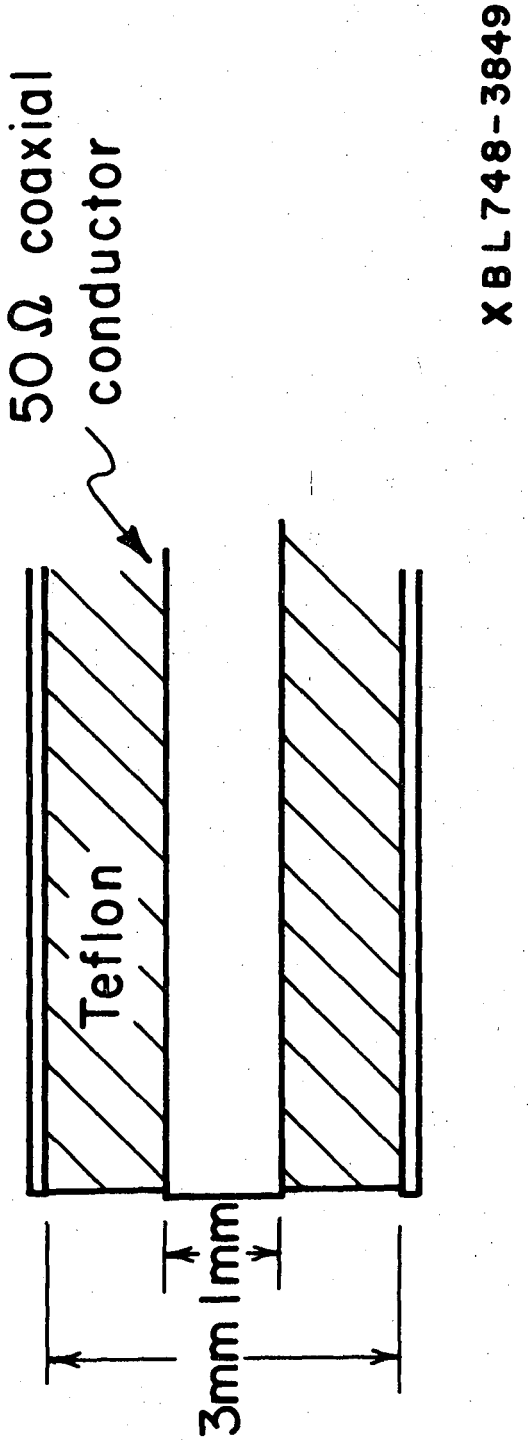

XBL748-3849

Fig. 29

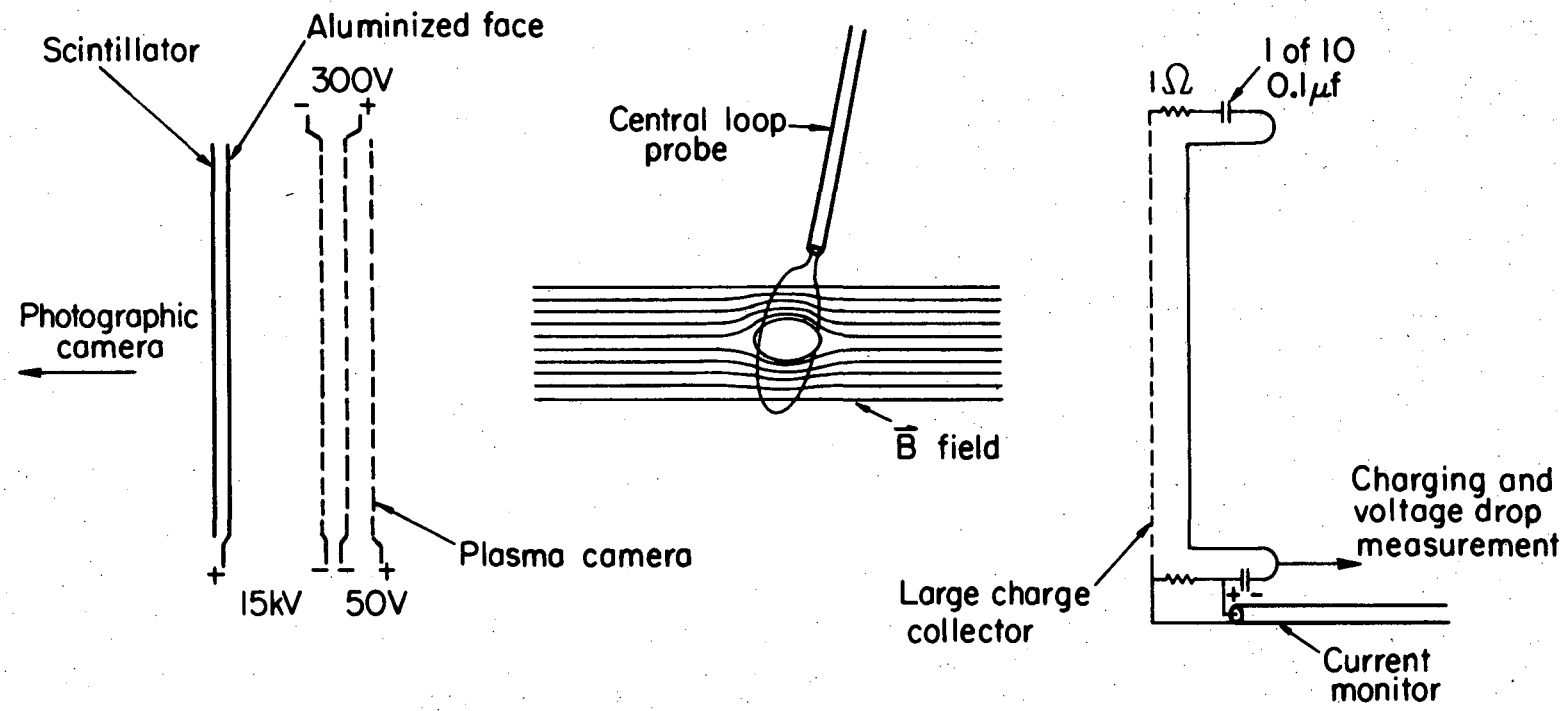

XBL748-3865

Fig. 30

0 0 0 0 4 1 0 8 1 7 3

LEGAL NOTICE

This report was prepared as an account of work sponsored by the United States Government. Neither the United States nor the United States Atomic Energy Commission, nor any of their employees, nor any of their contractors, subcontractors, or their employees, makes any warranty, express or implied, or assumes any legal liability or responsibility for the accuracy, completeness or usefulness of any information, apparatus, product or process disclosed, or represents that its use would not infringe privately owned rights.

TECHNICAL INFORMATION DIVISION
LAWRENCE BERKELEY LABORATORY
UNIVERSITY OF CALIFORNIA
BERKELEY, CALIFORNIA 94720